Icarus 455 (2026) 117099

Contents lists available at ScienceDirect

Icarus

journal homepage: www.elsevier.com/locate/icarus

Research paper

The paths that sculpt a comet: Quantifying the sediment trajectories shaping 67P's landscapes

Abhinav S. Jindal [a,*], Raphael Marschall [b,c], Nicholas Attree [d], Jason M. Soderblom [e], Björn J.R. Davidsson [f], Jean-Baptiste Vincent [g], Olivier Groussin [h], Orkan M. Umurhan [i,j], Jordan K. Steckloff [k,l], Samuel P.D. Birch [a]

[a] Department of Earth, Environmental, and Planetary Sciences, Brown University, Providence, RI, USA
[b] Centre National de la Recherche Scientifique, Laboratoire J.-L. Lagrange, Observatoire de la Côte d'Azur, Nice, France
[c] International Space Science Institute, Bern, Switzerland
[d] Instituto de Astrofísica de Andalucía (CSIC), Glorieta de la Astronomià s/n, Granada, Spain
[e] Department of Earth, Atmospheric and Planetary Sciences, Massachusetts Institute of Technology, Cambridge, MA, USA
[f] Jet Propulsion Laboratory, California Institute of Technology, Pasadena, CA, USA
[g] Institute of Planetary Research, Deutsches Zentrum für Luft und Raumfahrt, Berlin, Germany
[h] Aix Marseille Univ, CNRS, CNES, Laboratoire d'Astrophysique de Marseille, Marseille, France
[i] SETI Institute, Carl Sagan Center, Mountain View, CA, USA
[j] Planetary Systems Branch, Space Sciences Division, NASA Ames Research Center, Moffett Field, CA, USA
[k] Planetary Science Institute, Tucson, AZ, USA
[l] Department of Aerospace Engineering and Engineering Mechanics, University of Texas at Austin, Austin, TX, USA

ARTICLE INFO

Dataset link: https://psa.esa.int/psa, https://github.com/abhinav-s-jindal/67P_sediment_transport_pathways

Keywords:
Comets(280)
Small solar system bodies (1469)
Comet nuclei (2160)
Comet surfaces (2161)
Planetary geology (2288)

ABSTRACT

Cometary surfaces exhibit striking morphological diversity, with thick, smooth deposits abruptly transitioning to exposed bedrock and cliffs. This heterogeneity reflects spatially variable sublimation-driven erosion and sediment transport, yet how these processes combine to sculpt cometary surfaces remains poorly understood. Here, we investigate these dynamics on comet 67P/Churyumov–Gerasimenko by numerically modeling the ballistic trajectories of ejected particles over multiple ejection–deposition cycles. We find that the comet's morphology can be explained by three fundamental dynamical regimes: *collectors*, where sediment trajectories converge and sediment accumulates; *shadow zones*, which are sheltered from incoming sediment; and *ejectors*, which rapidly lose sediment to space. Their spatial arrangement, controlled primarily by the nucleus's shape, spin-axis orientation, and rotation period, reproduces the observed distribution of surface morphologies with striking fidelity. These results demonstrate that cometary landscapes, and the evolution of their comae, arise from the coupling between ballistic sediment transport and nucleus geometry.

1. Introduction

The formation of smooth regolith deposits via sediment transport on comets was first proposed over three decades ago (Möhlmann, 1994). The Deep Space 1 flyby of comet 19P/Borrelly in 2001 provided the first clear indication of such mantling, revealing broad, smooth deposits draped across the comet's nucleus (Soderblom et al., 2002). While these early observations hinted that loose material could be mobilized and redistributed across cometary surfaces, the underlying processes remained uncertain. A more definitive picture emerged during the Deep Impact flyby of comet 9P/Tempel 1 in 2005, which revealed large patches of smooth material in gravitational lows (A'Hearn et al., 2005; Thomas et al., 2007). The morphology of these smooth deposits led to speculation that they were "flows" of material, possibly fluidized and suspended by gas released from the comet's interior (Thomas et al., 2007; Belton and Melosh, 2009). This interpretation was later challenged by EPOXI (Extrasolar Planet Observation and Deep Impact Extended Investigation) observations of comet 103P/Hartley 2 in 2010, where ice-rich sediment ejected from the comet's small lobe appeared to settle into gravitational lows in the smooth "waist" of the nucleus (A'Hearn et al., 2011). Indeed, subsequent analysis showed that a large fraction of these icy chunks travel below escape speed and eventually re-deposit on the surface (Hermalyn et al., 2013), where they could be re-mobilized—thereby explaining both morphological and spectroscopic observations (A'Hearn et al., 2011; Thomas et al., 2013).

* Corresponding author.
E-mail address: abhinav_jindal@brown.edu (A.S. Jindal).

https://doi.org/10.1016/j.icarus.2026.117099
Received 6 February 2026; Received in revised form 30 March 2026; Accepted 11 April 2026
Available online 16 April 2026

The Rosetta mission to comet 67P/Churyumov–Gerasimenko (hereafter, 67P) further clarified this picture, as its high spatial resolution (as high as ~10 cm px^{-1} from orbit) and long baseline of observations (over 2 years) captured the evolution of a cometary landscape in unprecedented detail. At the largest scale, Rosetta observed two dominant morphological terrain types (Birch et al., 2017; Vincent et al., 2017; Thomas et al., 2018). Largely restricted to the southern hemisphere are the "consolidated" terrains (Fig. 1A,B)—exposed bedrock, often with networks of fractures across their surface (El-Maarry et al., 2015). Many higher-slope consolidated terrains also show evidence of crumbling and mass-wasting, either directly through observed changes (Pajola et al., 2017a; El-Maarry et al., 2019) or indirectly through boulder deposits immediately downslope (Pajola et al., 2015). There are also vast sedimentary deposits of cm–dm-sized particles termed "smooth" terrains (Fig. 1C–F). 67P's smooth terrains are mostly located in the northern hemisphere, largely within select global gravitational lows. In some areas (Fig. 1C), thick accumulations of sediment fully bury the underlying bedrock, forming expansive, ponded deposits. In others (Fig. 1E,F), the mantle is thin enough for the underlying structure of the consolidated terrains to remain visible (Thomas et al., 2015b; Birch et al., 2017) and even outcrop in isolated locations.

As on other planetary bodies, the smooth terrain sediment is likely eroded from the underlying bedrock. This is consistent with the high-resolution images from the Philae lander, which showed the bedrock comprises a mixture of fine-grained material — featureless at the ~1 mm px^{-1} scale of ROLIS images — and coarser fragments broken into mm–dm-sized particles, not unlike a conglomerate rock on Earth (Bibring et al., 2015, Fig. 1B). Erosion on comets occurs via the sublimation of near-surface ices, combined with the thermophysical breakdown of the material itself over repeated heating/cooling cycles (Birch et al., 2017; El-Maarry et al., 2019). Similar thermal-fatigue processes also operate on asteroids, where they can mobilize cm-scale particles (Molaro et al., 2020). In the cometary context, the interplay between microgravity and sublimation-driven gas drag allows eroded sediment to be lofted from the surface and transported ballistically across the nucleus—though the precise mechanisms and ejection velocities remain poorly constrained (Vincent et al., 2019). Indeed, Rosetta observations showed that sediment ejection likely occurs across the entire nucleus, either by being initially released from the consolidated terrains or re-ejected from smooth terrains (Thomas et al., 2015a; Keller et al., 2017). As on Hartley 2, Rosetta observed that a significant fraction of cm–dm-sized sediment ejected from the nucleus "snows" down across the surface, at varying rates and times (Rotundi et al., 2015; Thomas et al., 2015a; Agarwal et al., 2016; Keller et al., 2017). This ballistic sediment transport process, therefore, builds up the diverse smooth terrain deposits observed across the comet.

The global-scale smooth–rough terrain dichotomy we observe today reflects 67P's current orbital and spin configuration—the southern hemisphere receives far more intense insolation than the north (Keller et al., 2015, 2017; Hu et al., 2017). Because sublimation rates, and therefore erosion and outgassing rates, scale exponentially with temperature (Steckloff et al., 2015), most of the erosion occurs in the months surrounding perihelion, with limited (albeit nonzero) activity during the rest of the orbit. As a result, erosion rates are much higher in the south, generating and ejecting more sediment. Higher outgassing rates also limit sediment fall back, preferentially re-ejecting material before it can deposit (Marschall et al., 2020). In contrast, the north is in polar winter during perihelion, with minimal outgassing, which permits deposition. During any ejection event, this transportable material can also retain its volatile ices, depending on the particle size, temperature, and flight time (Davidsson et al., 2021). For the typical cm–dm-sized grains of smooth terrains (Fig. 1D), a significant fraction of the initial volatile content is preserved throughout any given ejection event (Davidsson et al., 2021). As on Hartley 2, these volatiles can then be reactivated post-deposition when the northern deposits are next illuminated. For 67P's current orbit, this would occur during the comet's next inbound passage, consistent with the notable pre-perihelion activity observed within these deposits early in Rosetta's mission (Lara et al., 2015).

While this framework qualitatively describes the broad global-scale patterns on 67P, Rosetta observations reveal pronounced local and regional variability in both the erosion and deposition of smooth terrain deposits (Barrington et al., 2023; Jindal et al., 2024). For instance, on the northern "tops" of both lobes (within the regions of Ash and Ma'at) where the smooth terrain deposits are thinnest, no surface changes were detected during the mission (Figure 12 in Barrington et al. (2023)). Models to explain ROSINA measurements (Marschall et al., 2016) and non-gravitational accelerations (Kramer et al., 2019; Attree et al., 2023) also indicate minimal activity from these regions. By contrast, large-scale changes driven by scarp migration were observed in thicker smooth terrain deposits (Groussin et al., 2015; El-Maarry et al., 2017; Birch et al., 2019; Davidsson et al., 2022; Jindal et al., 2022), consistent with a more volatile-rich near-surface. Some of these active smooth terrains were even located at high northern latitudes (Birch et al., 2019; Davidsson et al., 2022), similar to Ash and Ma'at (e.g., Hapi). This contrast indicates that activity patterns cannot be explained solely by post-emplacement volatile depletion. Although local topography can lead to variable insolation patterns (Jindal et al., 2022), the heterogeneity in activity implies further differences in the dust mantle thickness, which is directly related to the origin and transport history of sediments. Furthermore, pre- and post-perihelion comparisons show that deposition is not in the form of a uniform blanket (Jindal et al., 2024). Instead, it varies significantly across the comet, again suggesting complex and spatially variable sediment transport pathways. Therefore, despite the overall south-to-north sediment migration driven by seasonal insolation patterns, we still lack understanding of (i) the specific sediment transport pathways across 67P, (ii) the role that 67P's shape and topography play in dictating these pathways, and (iii) how sediment may evolve while in transit along these pathways. Each of these factors then governs the long-term distribution and reactivation potential of 67P's landscapes.

Recent modeling has begun to quantify these effects by explicitly tracking ballistic motion of particles across 67P's irregular, rotating nucleus. Kloos et al. (2025), for example, combined thermophysical estimates of time-variable activity with Monte Carlo simulations of particle trajectories, demonstrating that the interplay between topography, gravity, and rotation can produce strongly heterogeneous fallback patterns, beyond what is expected from seasonal insolation alone. In their approach, particles are ejected assuming a uniform distribution of launch speeds, such that the resulting deposition patterns represent the superposition of transport operating across multiple dynamical regimes. While this treatment captures orbit-scale mass redistribution, the use of a velocity distribution means that distinct modes of transport — with potentially different efficiencies, spatial extents, and geomorphic consequences — are convolved in the resulting patterns. Given that the mechanism through which sediment is ejected is unknown (Fulle et al., 2019; Gundlach et al., 2020; Keller and Kührt, 2020; Bischoff et al., 2023; Attree et al., 2024, 2025; Schuckart and Blum, 2025), resolving sediment transport as a function of launch speed is therefore essential for identifying the underlying, specific transport pathways, sinks, and barriers that govern where material accumulates, where it remains mobile, and how smooth terrains evolve over time.

To address this gap, we use a ballistic transport model to investigate sediment redistribution across 67P over an orbital timescale, with transport resolved as a function of launch speed. By isolating distinct velocity regimes, we examine how the nucleus shape, gravity field, and rotation organize sediment transport and control where material is preferentially redistributed. We show that this velocity-resolved framework reproduces both the large-scale distribution of smooth terrains and the observed spatial patterns of activity and inactivity, indicating that ballistic sediment transport is a primary mechanism governing the organization of cometary landscapes. This framework provides a physically grounded basis for interpreting the evolution of 67P's surface

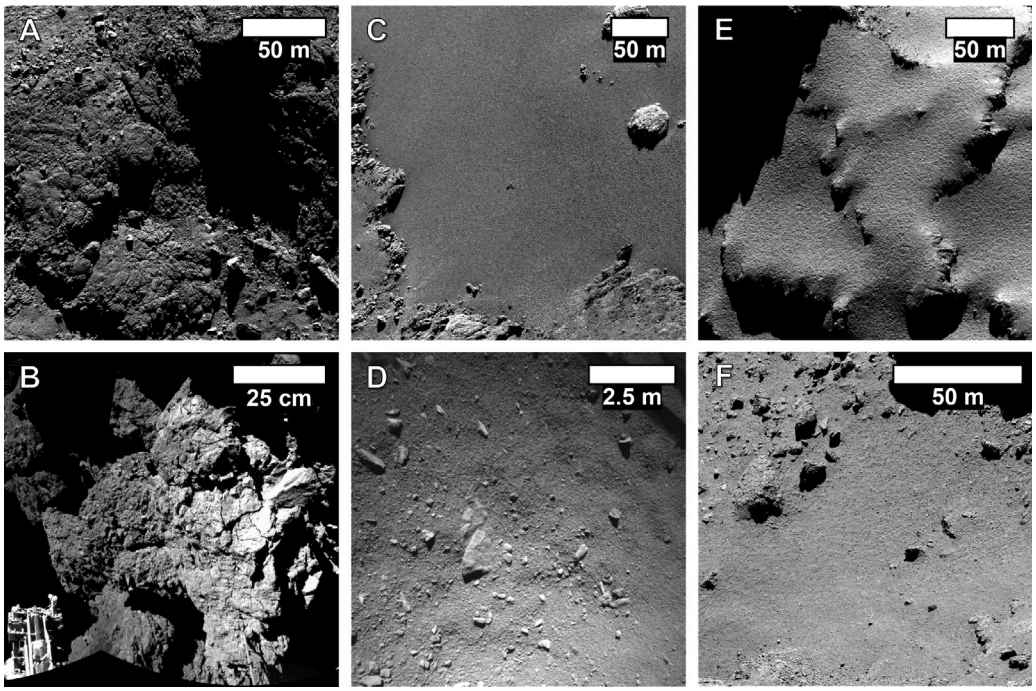

Fig. 1. Representative surface morphologies on comet 67P, showcasing the range of terrains our model seeks to reproduce through organized sediment-transport pathways. (A) Consolidated, fractured bedrock exposing polygonal and blocky textures. (B) Fine-scale view of fractured, consolidated material from Philae's CIVA panorama (Bibring et al., 2015). (C) Smooth terrain deposit in the Imhotep region, thick enough to bury the underlying topography. (D) High-resolution view of a smooth terrain deposit from Philae ROLIS during descent (Mottola et al., 2015), revealing a granular surface texture with cm–dm-sized sediment. (E) In some regions (e.g., Ash), smooth terrain mantling is thin, allowing the large-scale structure of the substrate to remain visible. (F) Thin sediment accumulation and a boulder field at the base of a cliff, suggesting a continuous process of mass wasting.

and provides context for future investigations, including sample site selection for proposed sample return missions such as CAESAR (Squyres et al., 2018). More broadly, because our results demonstrate that large-scale topography exerts a first-order control on the distribution and reactivation of smooth terrains, this approach provides a useful framework for interpreting surface evolution on other comets explored by spacecraft.

2. Methods

We investigate long-term sediment redistribution on 67P using a ballistic transport framework that combines velocity-dependent particle trajectories with spatially varying ejection probabilities. For a discrete set of launch speeds, we first compute surface-to-surface ballistic sediment transport pathways. These calculations quantitatively describe where particles launched from any given location can travel across the nucleus under the influence of gravity and rotation (Section 2.1). These pathways are then weighted by a location-dependent ejection probability derived from orbit-integrated erosion models (Section 2.2) and applied iteratively to simulate repeated re-ejection and multi-hop transport (Section 2.3).

Each launch speed is modeled independently, allowing velocity-dependent transport behavior to be isolated without assumptions about the underlying ejection velocity distribution and/or particle size distribution. Rather than representing any individual transport episode, the resulting particle distributions are interpreted as the asymptotic outcome of repeated ballistic redistribution over long timescales. This approach enables identification of persistent transport pathways, depositional sinks, and regions that remain largely inaccessible to ballistic motion.

2.1. Ballistic transport model

We use the DRAG3D code (Marschall et al., 2016) to model ballistic sediment transport across the surface of 67P. The shape of the nucleus is represented using the SHAP7 model (Preusker et al., 2017), reduced to ~440,000 facets to optimize computational efficiency while preserving the ~decameter-scale surface slopes that strongly influence particle trajectories.

The physics of sediment ejection from cometary surfaces remains poorly constrained (Fulle et al., 2019; Gundlach et al., 2020; Keller and Kührt, 2020; Bischoff et al., 2023; Attree et al., 2024, 2025; Schuckart and Blum, 2025). Our focus here is on the motion of particles after they have been accelerated to their launch velocity, independent of the specific acceleration mechanism. Specifically, our work focuses on the transport of particles in the cm–dm size range, consistent with observations of smooth terrains (Pajola et al., 2016, 2017b). We do not impose an explicit size distribution within this range. Instead, our approach is deliberately agnostic to particle size and ejection mechanism, focusing on post-launch ballistic motion over a range of ejection velocities.

This size range was also chosen because such particles are large enough to not be coupled to the gas flow — unlike finer dust (Thomas et al., 2015a) — yet small enough to be mobilized during active periods (Rotundi et al., 2015; Agarwal et al., 2016). Therefore, we assume that, once the particles have been accelerated to their given launch velocity, coma densities are low enough that gas drag does not affect their subsequent motion. However, neglecting gas drag remains an approximation. Gas–dust interactions during fallback can induce lateral drift and modify the resulting deposition pattern, particularly for smaller particles or in regions of stronger outgassing, such as the southernmost latitudes near perihelion (Section 3.5). Our results should therefore be interpreted as a first-order model of post-launch sediment routing for relatively large particles that dominate the observed distribution within smooth terrains, rather than a complete description of dust dynamics in the near-nucleus coma.

Once launched, particle motion is therefore governed solely by the comet's gravity and the Coriolis and centrifugal forces arising in the rotating frame. For a particle at position $\mathbf{x}$ with velocity $\mathbf{v}_p = \frac{d\mathbf{x}}{dt}$, the

equation of motion is:

$$\frac{d^2\mathbf{x}}{dt^2} = \mathbf{a}_G + \mathbf{a}_C \tag{1}$$

where $\mathbf{a}_G$ is the gravitational acceleration, and $\mathbf{a}_C$ is the combined Coriolis and centrifugal acceleration. The gravitational field is approximated by discretizing the SHAP7 model to 2 million volume elements of constant density, $\rho = 535\ \mathrm{kg\,m^{-3}}$ (Pätzold et al., 2019):

$$\mathbf{a}_G(\mathbf{x}) = G\rho\Delta V \sum_n \frac{\mathbf{r}}{|\mathbf{r}|^3} \tag{2}$$

where $\mathbf{r}$ is the vector from point $\mathbf{x}$ to each volume element ΔV. The rotational accelerations are given by:

$$\mathbf{a}_C(\mathbf{x}) = -2(\boldsymbol{\omega} \times \mathbf{v}_p) - \boldsymbol{\omega} \times (\boldsymbol{\omega} \times \mathbf{x}) \tag{3}$$

where $\boldsymbol{\omega}$ is the rotation velocity of the comet. Although 67P's rotation rate changed slightly during Rosetta's escort phase (by $\sim$ 3%; Jorda et al. (2016)), for simplicity, we hold it constant at $\sim$ 12 h.

We simulate trajectories for ejection velocities ranging from 0.1 to 0.9 $\mathrm{m\,s^{-1}}$ in increments of 0.1 $\mathrm{m\,s^{-1}}$. The lower bound corresponds to short hops that deposit material near the source, while the upper bound approaches escape speed, above which most particles are lost (Braga et al., 2025). The model is initialized with ~50 million test particles uniformly distributed across the surface (one for every square meter), effectively assuming sediment is available for transport on every facet so that all regions can contribute to the modeled transport network. Particles are then randomly ejected within a cone of 5° apex angle centered along the local surface normal and are tracked until they either re-impact the surface or exceed the comet's Hill sphere radius (R_H),

$$R_H = d_\odot \left(\frac{M_n}{M_\odot}\right)^{\frac{1}{3}} \tag{4}$$

where $d_\odot$ is the heliocentric distance. For 67P, R_H varies from ~220 km at perihelion to ~1000 km at aphelion. Since sediment transport is concentrated near perihelion (Keller et al., 2017; Barrington et al., 2023), we adopt a cut-off of 300 km; particles crossing this boundary are considered lost to the comet's tail and trail. For computational efficiency, facets whose launch trajectories would exceed this Hill sphere cut-off at a given velocity are treated as incapable of launching material at that speed. Accordingly, they are initialized with no particles available for ejection in that velocity bin. If such facets later receive sediment from other regions, this material is retained throughout the simulation (including during the multiple-hop iterations described below), even though in reality it would likely escape the system. In our interpretation of the results, any material deposited on these facets is treated as effectively lost from the system, since these regions are not permitted to re-eject sediment once it is deposited. This treatment has a negligible effect at low velocities but becomes important at higher velocities ($> 0.5\ \mathrm{m\,s^{-1}}$), where escape probabilities increase significantly.

This framework yields global, velocity-dependent surface-to-surface transport maps, revealing how topography, rotation, and gravity combine to control where sediment from any given source region can be delivered. While these maps initially represent single-hop transport, they can be applied iteratively to simulate multi-hop redistribution (Section 2.3), where particles are re-ejected from their initial landing sites and travel further across the surface. This capability is particularly important when combined with spatially varying ejection probabilities, as it enables modeling of progressive sediment dispersal over an orbital cycle.

2.2. Ejection probability

We assume sediment is uniformly available across 67P's surface, but the actual rate at which material is mobilized varies strongly with location due to differences in net insolation. To account for this, we use the cumulative erosion map from Groussin et al. (2025), in which erosion was modeled over a full orbital period for a 300,000-facet shape model using a pure-water–ice sublimation framework, i.e., erosion/ejected solid mass is directly proportional to sublimated water mass. Their calculations incorporate the nucleus' shape, spin state, and heliocentric distance-dependent illumination geometry, and the resulting erosion rates were rescaled to match observed water production during Rosetta's escort phase. This provides a physically motivated proxy for the integrated sediment loss potential of each facet.

We interpolate this erosion map onto our ~440,000-facet model. Although the map does not capture seasonal timing of erosion (e.g., the pre-perihelion dominance of erosion in the Hapi region versus the post-perihelion dominance in the southern hemisphere), it is well suited for modeling redistribution over the entire orbit. We convert the erosion map to an ejection probability map by normalizing values to the range 0–1 (Fig. 2). Over 95% of facets still have a minimum ejection probability of 0.1 such that they remain at least minimally active, maintaining global connectivity in the iterative simulations. Facets with a probability of 1 are the most erosive, though they may still experience net accumulation if more trajectories terminate on them than originate from them.

By combining this ejection probability map with the ballistic transport model described above, we can weight each simulated trajectory by the likelihood of sediment being launched from its source location. This probability-weighted framework sets the stage for our iterative ballistic transport simulations, in which particles can undergo multiple hops, progressively redistributing material in a manner consistent with both transport pathways and spatial variations in erosion potential.

2.3. Iterative ballistic transport

Repeated hopping along ballistic transport pathways will, over time, concentrate sediment in some regions while depleting it from others (Fig. 3). Given fixed transport pathways at a given velocity, the redistribution pattern approaches a steady configuration that represents the asymptotic outcome of repeated ballistic transport over long timescales, rather than individual ejection events. By simulating this process for each velocity separately, we can map the asymptotic "sinks" and "sources" of sediment, providing insight into the long-term consequences of ballistic transport without requiring assumptions about the actual velocity distribution or the number of hops. For a given iteration, the flux from a source facet i to a destination facet j is computed as:

$$F_{i\to j} = \frac{N_{avail}(i)}{N_{dest}(i)} \times P_{ej}(i) \times n_{ij} \tag{5}$$

where $N_{avail}(i)$ is the number of particles available to eject from facet i, $N_{dest}(i)$ is the number of unique trajectories out of i, $P_{ej}(i)$ is the ejection probability of i, and n_{ij} is the number of trajectories from i that land in j at that velocity.

Each velocity is iterated independently, allowing us to isolate redistribution patterns for that launch speed. This approach assumes that particles from any given region could, in principle, be ejected at any velocity within our modeled range. However, because we lack constraints on the true velocity distribution, we remain agnostic regarding how often each speed occurs and instead explore the steady-state pattern that results for each discrete velocity.

Each simulation is run for 1000 iterations. We only report results up to 100 iterations because by that point the particle distribution changes by less than 1% between successive iterations across all velocity bins. Nevertheless, the full 1000-iteration outputs are provided in the accompanying data products for completion. One simplifying assumption we make is that particles can land and remain on any surface, including steep slopes or overhangs. In reality, deposits on steep slopes are likely unstable and would rapidly move downslope. In our framework, this downslope motion is effectively represented by the lower-velocity hops, which tend to deposit material in the local gravitational lows.

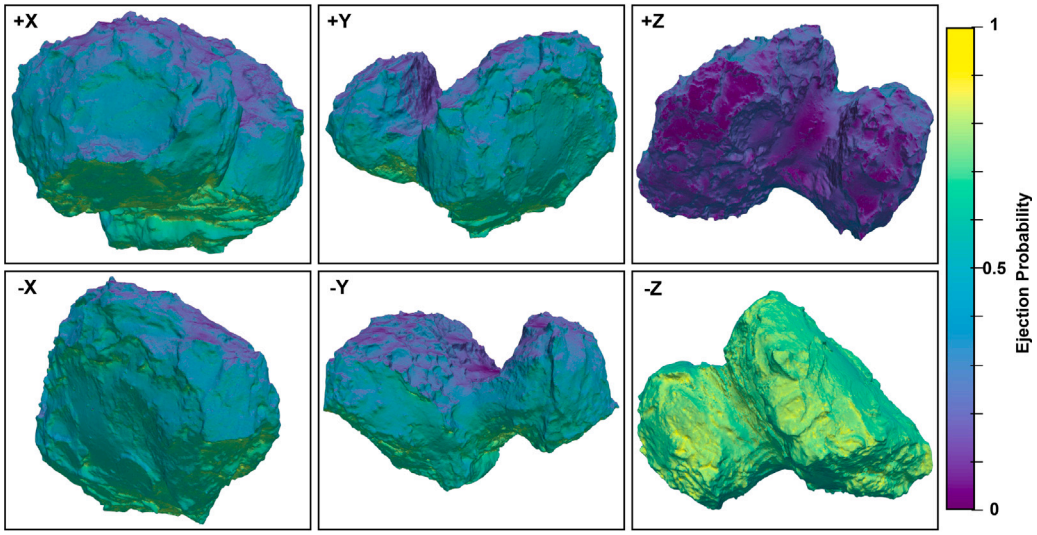

Fig. 2. Global ejection probability map for comet 67P. Ejection probability derived from the thermophysical model of Groussin et al. (2025), scaled between 0 (minimum) and 1 (maximum). Each panel shows the probability of particle ejection across 67P's surface, viewed along the six principal axes of the comet. This probability field serves as the input weighting for our multi-hop sediment transport simulations, controlling the likelihood of sediment mobilization from each facet.

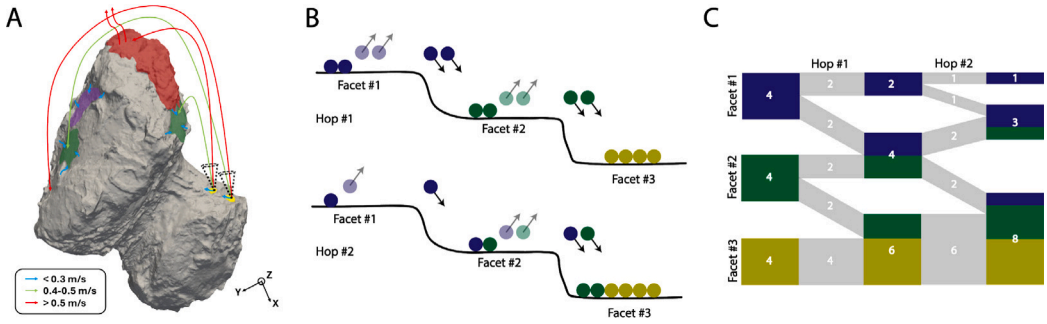

Fig. 3. Schematic overview of the sediment transport framework. (A) Conceptual illustration of the three dynamic terrain types that emerge from our simulations. Green regions represent *collectors*, which intercept and retain incoming particles; purple regions denote *shadow zones*, which remain sheltered from incoming trajectories; and red regions indicate *ejectors*, where sediment is preferentially lost to space. Example particle trajectories are shown for three velocity regimes: low (<0.3 $\mathrm{m\,s^{-1}}$, cyan), intermediate (0.4–0.5 $\mathrm{m\,s^{-1}}$, green), and high (>0.6 $\mathrm{m\,s^{-1}}$, red). As ejection velocity increases, trajectories extend farther and increasingly escape the comet's gravitational influence. (B) Simplified illustration of sediment exchange between three representative facets. Facet #1 loses material due to its moderate ejection probability ($P_{ej} = 0.5$) and absence of incoming particles; Facet #2 also loses material, though more gradually, as it both receives sediment from Facet #1 and ejects with $P_{ej} = 0.5$; Facet #3 gains sediment because it receives flux from Facet #2 but does not eject ($P_{ej} = 0$). (C) Schematic depiction of how these exchanges evolve through successive hops. Over time, sediment is progressively removed from Facets #1 and #2 and accumulates on Facet #3, illustrating how local probabilistic exchanges give rise to global patterns of erosion, deposition, and steady-state sediment distribution across the comet's surface. (For interpretation of the references to color in this figure legend, the reader is referred to the web version of this article.)

By treating each velocity independently and iterating until near convergence, we obtain an estimate of the asymptotic redistribution of particles—showing where sediment is most likely to accumulate or be lost over long timescales under the combined influence of ballistic pathways and spatial variations in ejection probability.

3. Results

Sediment redistribution on 67P is strongly controlled by ejection velocity, with distinct transport regimes emerging across the modeled velocity range. As launch speeds increase, transport transitions from highly localized motion confined by local topography, to basin-scale accumulation in global gravitational lows, and ultimately to near-global redistribution and loss to space. In the sections below, we describe how these regimes evolve across ejection velocities of 0.1–0.9 $\mathrm{m\,s^{-1}}$, highlighting the characteristic pathways, sinks, and loss processes that define each regime. For reference, the average escape velocity of 67P is $v_{\mathrm{esc}} = \sqrt{2GM_n/R_n} = 0.83\ \mathrm{m\,s^{-1}}$, where the mass of the nucleus is $M_n = 9.982 \times 10^{12}$ kg (Pätzold et al., 2019) and the area-equivalent nucleus radius is $R_n = 1932$ m (Jorda et al., 2016).

At the lowest modeled ejection velocities (0.1–0.2 $\mathrm{m\,s^{-1}}$), particle motion is strongly constrained by the local topography. Particles deposit into nearby gravitational lows, unable to escape their immediate local basins (Fig. 4; Movies C.16–C.17). These local "catchments" retain material within a limited area, even after hundreds of hops, implying that sediment mobilized at these speeds cannot modify the global-scale distribution of sediment. Instead, motion at these low velocities likely only influences the textures superposed on the smooth terrain deposits (Keller et al., 2017; Jindal et al., 2024).

At slightly higher velocities (0.3–0.4 $\mathrm{m\,s^{-1}}$), trajectories extend beyond local topographic lows but remain concentrated around global gravitational lows. These regions act as long-term sediment sinks, concentrating material over multiple hops. At 0.3 $\mathrm{m\,s^{-1}}$, the vast majority of trajectories terminate in these global lows, while at 0.4 $\mathrm{m\,s^{-1}}$ a noticeable fraction of particles reach other parts of the nucleus, though the global lows still dominate as accumulation zones (see Figs. C.18–C.19).

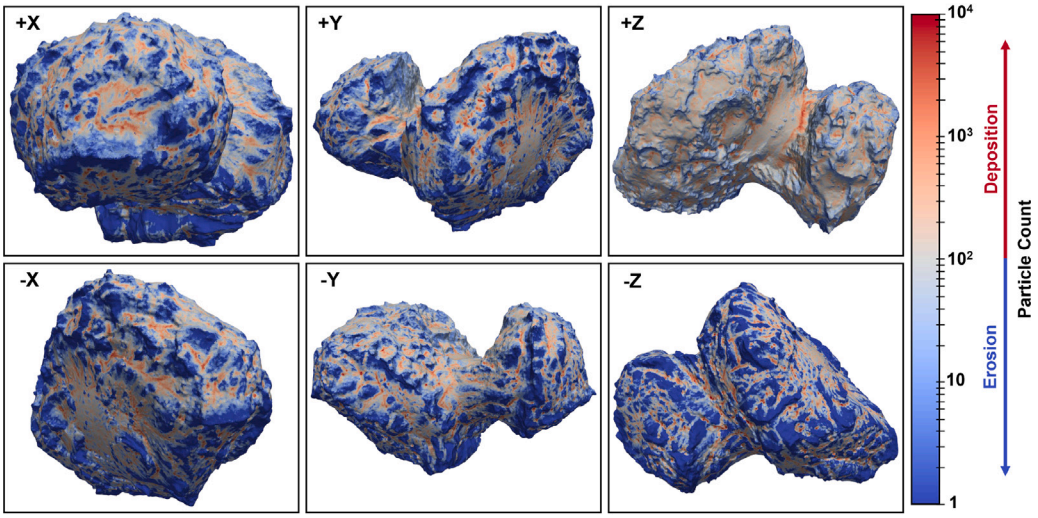

Fig. 4. Local sediment redistribution at low ejection velocity. Results of simulations initialized with ~100 particles per facet, showing the number of particles remaining on each facet of 67P's shape model after 10 hops at an ejection velocity of 0.1 $m\,s^{-1}$. Red tones indicate net particle gain (deposition), while blue tones indicate net particle loss (erosion). Each panel shows the outcome viewed along one of the six principal axes of the comet. At these low velocities, particle motion remains locally confined: sediment drains from steep slopes and accumulates within adjacent topographic lows, where it becomes trapped after repeated hops. (For interpretation of the references to color in this figure legend, the reader is referred to the web version of this article.)

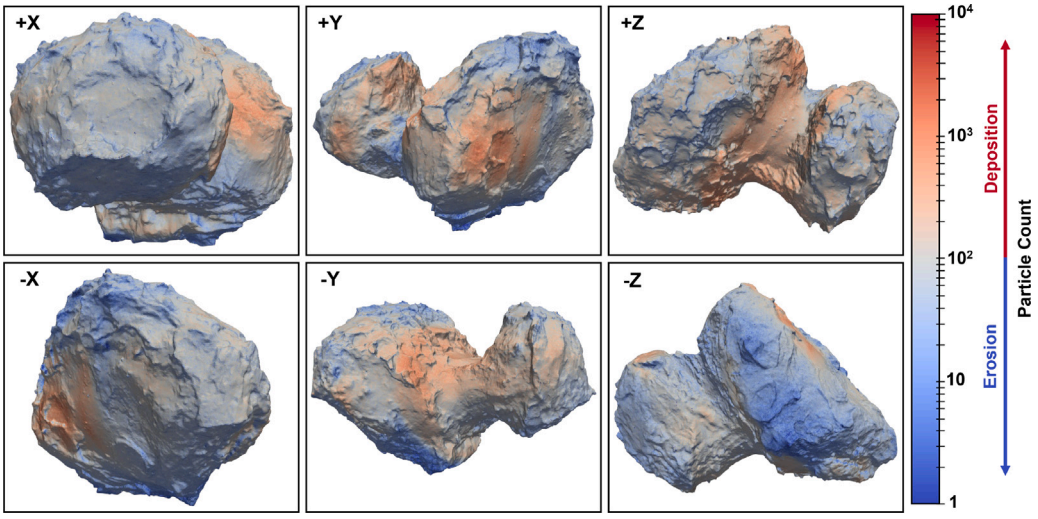

Fig. 5. Global sediment redistribution at moderate ejection velocity. Results of simulations initialized with ~100 particles per facet, showing the number of particles remaining on each facet of 67P's shape model after 10 hops at an ejection velocity of 0.5 $m\,s^{-1}$. Figure layout is the same as Fig. 4. At this velocity, sediment transport transitions from locally confined motion to near-global redistribution driven primarily by the comet's shape and rotation. Regions that intercept and accumulate material act as "collectors," while those shielded from incoming trajectories form "shadow zones" with minimal deposition. These interactions establish the global sediment pathways that connect 67P's distinct geomorphic units.

Once ejection speeds reach 0.5 $m\,s^{-1}$, transport undergoes a marked transition. Particles are no longer confined to local basins or global gravitational lows. Instead, sediment is fully redistributed across much of the nucleus (Fig. 5; Fig. C.20). In this regime, sediment pathways are increasingly shaped by the large-scale topography of the nucleus. Regions that intercept oncoming trajectories are termed "collectors" much like a windshield catching airborne debris. Anubis and the western margin of Imhotep are two examples of collectors. Flat collectors can accumulate material directly, whereas steeper topographic promontories are more likely to pass any acquired sediment load downslope to the nearest basin over time (we do not explicitly model this process; see Materials and Methods). Immediately beyond most promontories, "shadow zones" form where the sediment flux sharply drops because trajectories are intercepted upstream. As the nucleus rotates beneath the lofted particles, those that clear the promontory land farther downrange, leaving the intervening region starved of incoming sediment. Together, these promontory–shadow interactions define the redistribution pattern unique to this velocity regime, producing both concentrated sinks and sharp low-flux gaps across the comet's surface.

At the highest modeled velocities (0.6–0.9 $m\,s^{-1}$), sediment redistribution becomes weakly organized, with trajectories largely insensitive to both local and large-scale confinement. As a result, the dense convergence patterns seen at lower velocities give way to a sparser, more scattered distribution of particles across the surface. More striking is that certain facets with the highest tangential velocities — typically near the rotational equator — act as persistent "ejectors". Such facets eject a substantial fraction of sediment beyond the comet's Hill sphere, where it is lost. Many of these ejectors coincide with promontories, whose protruding geometry enhances tangential velocity. Observationally, such promontories are steep with exposed bare bedrock, consistent

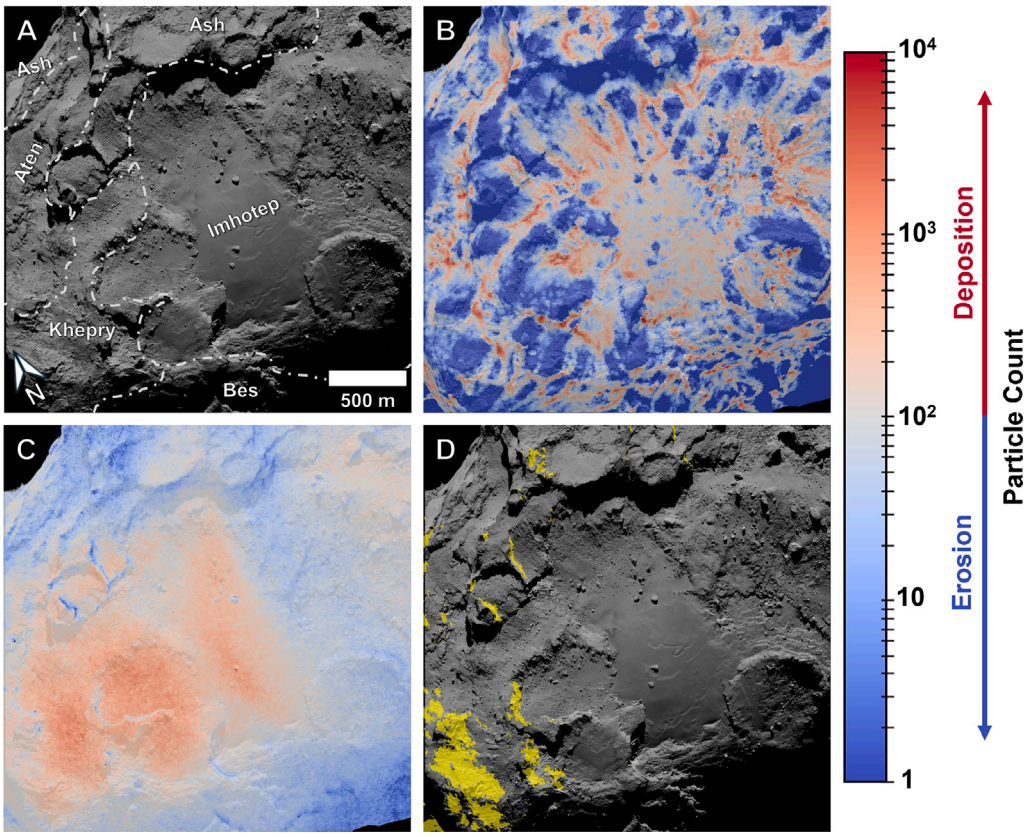

Fig. 6. Sediment redistribution in the Imhotep region. (A) OSIRIS NAC image of the large lobe showing the Imhotep basin and adjacent terrains, with regional boundaries labeled. Imhotep hosts the largest continuous smooth terrain deposit on 67P (Auger et al., 2015). (B) Modeled sediment redistribution at low ejection velocity (0.1 m s^{-1}, after 10 hops). Sediment drains from surrounding cliffs and settles within adjacent basins, where it becomes trapped—explaining the persistence of smooth material in these lows and the lack of mantling on neighboring slopes. (C) Redistribution at intermediate ejection velocity (0.5 m s^{-1}, after 10 hops). The central basin and western alcoves act as major "collectors," while a pronounced "shadow zone" forms in the pitted eastern margin, where trajectories are intercepted upstream. (D) "Ejector" facets at high ejection velocity (0.7 m s^{-1}) highlighted in yellow. Large portions of Khepry transition into ejectors at higher velocities, consistent with the limited mantling observed in this region. Together, these modeled collectors, shadow zones, and ejector regions closely reproduce the observed distribution of smooth and consolidated terrains across Imhotep.

with their role as ejectors. Therefore, over many hops ejectors become focused mass-loss facets, progressively draining material from the system to the coma and beyond (Figs. C.21–C.24).

In reality, each ballistic hop is randomly sampled from a distribution of possible launch velocities, that eject a distribution of particle sizes, both of which vary across the surface and over time, depending on local activity and illumination histories. Determining this velocity distribution is an outstanding problem (Vincent et al., 2019) that is beyond the scope of this study. Instead, our simulations isolate the redistribution patterns that would arise if particles were repeatedly ejected at a single velocity. This enables us to link specific morphological outcomes to distinct transport regimes. Notably, ~0.5 m s^{-1} emerges as the dominant velocity for global sediment redistribution. Below this threshold, particles tend to remain confined—either trapped in local topographic lows (0.1–0.2 m s^{-1}) or strongly constrained by large-scale gravitational basins (0.3–0.4 m s^{-1}). Above this threshold, transport becomes more diffuse, with particles sparsely scattered across the nucleus, while ejectors also begin to dominate sending a substantial fraction of the material into the coma. In the following sections, we examine select regional patterns to show that the large-scale morphology of 67P can be explained, to first-order, by ballistic sediment transport.

3.1. The Imhotep region

Imhotep hosts the largest single smooth terrain deposit on 67P in both the central and western portions of the broad gravitational low (Auger et al., 2015; Birch et al., 2017). The rotation of the nucleus means that sediment is transported into Imhotep preferentially from the east. Some sediment also leaks into Imhotep from southern regions, though to a lesser extent. At 0.5 m s^{-1}, sediment moving into the region first encounters promontories in Atum, Anubis, Apis, and Khepry. Sediment that does cross these topographic barriers either settles in the large central basin, in the western alcoves of the basin, or on the steep western slopes in the Khepry region. A shadow region appears in the pitted eastern margin of the basin, with only local trajectories capable of delivering sediment to the region (Fig. 6C). At low velocities (<0.5 m s^{-1}), sediment clears off steep slopes, flowing toward the central basin or getting trapped in alcoves (Fig. 6B). At the highest velocities (0.6–0.9 m s^{-1}), the steep western margin of the basin becomes an ejector region (Fig. 6D).

These simulations reproduce the observed distribution of terrain types with striking accuracy. The bulk of the sediment is deposited precisely where the thickest smooth terrain deposits are located, both within the central basin and within the western sediment-filled alcoves (Auger et al., 2015; Birch et al., 2017). We also capture local variations, such as the thinning of Imhotep's smooth deposit toward its eastern pitted terrains. In the eastern pitted region, there is only a thin mantling, which our simulations suggest can only be supplied by short-range down slope motion at lower velocities (0.1–0.2 m s^{-1}, Fig. 6B), consistent with documented local sediment migration in this region (Jindal et al., 2024). Finally, though the model predicts sediment accumulation on the smooth terrain-starved steep western slopes and

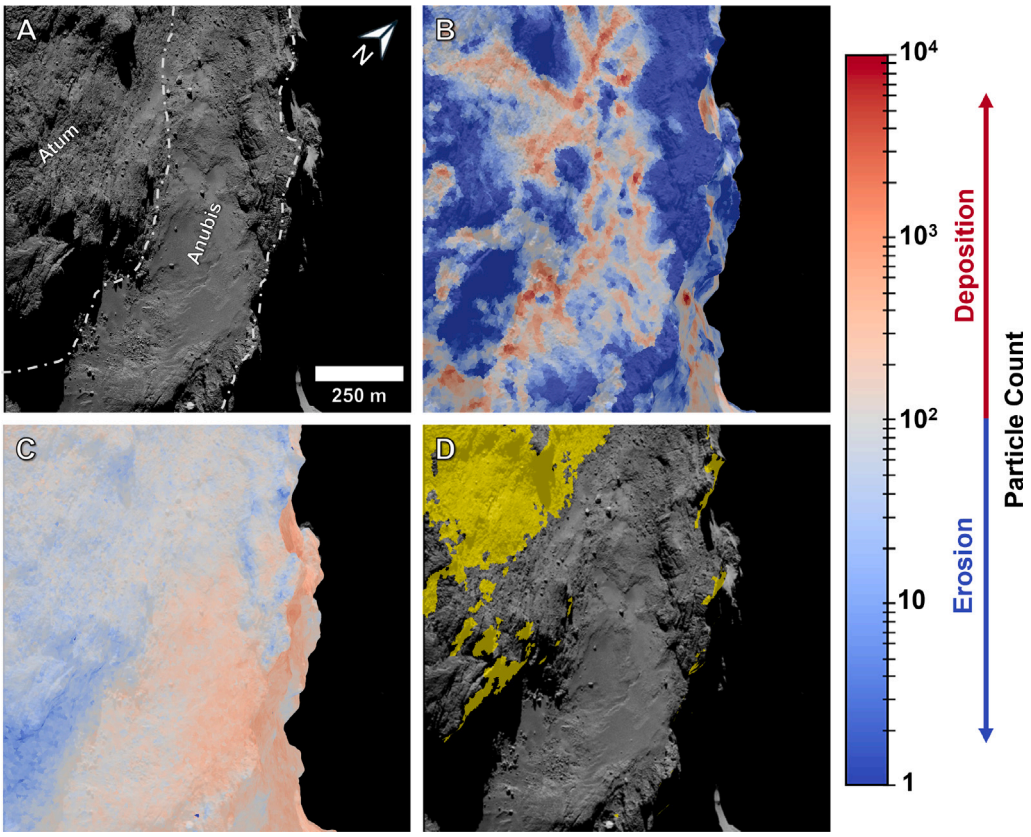

Fig. 7. Sediment redistribution in the Anubis–Atum region. (A) OSIRIS NAC image of the eastern margin of the large lobe, showing the Anubis smooth terrain deposit bordered by the consolidated terrains of Atum. (B) Modeled sediment redistribution at low ejection velocity (0.1 m s^{-1}, after 10 hops). Sediment drains from steep slopes and accumulates within nearby depressions, producing localized infill across both regions. (C) Redistribution at intermediate velocity (0.5 m s^{-1}, after 10 hops). In this regime, the southern and central portions of Anubis act as major "collectors", consistent with the thick smooth mantling observed there, while deposition decreases northward, matching the observed thinning of the unit. (D) "Ejector" facets at high ejection velocity (0.7 m s^{-1}) highlighted in yellow. Large portions of Atum transition into ejectors at higher velocities, explaining the persistence of consolidated, exposed bedrock. The modeled collectors and emerging ejector regions together reproduce the spatial gradient in smooth terrain thickness across Anubis and the scarcity of mantling in adjacent Atum.

Khepry at 0.5 m s^{-1}, these regions are mostly ejectors at higher velocities (Fig. 6D), hence any sediment delivered here would be relatively less stable. Furthermore, the steep slopes characteristic of these western cliffs would prevent stable accumulation, as material is more likely to bounce down slope into adjacent lows than to remain in place (an effect not captured by our model, which assumes sediment "sticks" to the surface upon landing).

3.2. Anubis, Atum, Serqet, and Bastet

Apart from western Imhotep, four other promontories emerge as major collectors of material in our simulations. These include Anubis and Atum on the eastern side of the large lobe, and Serqet and Bastet on the margins of the small lobe.

Anubis is a broad, low-lying region on the large lobe that hosts one of the most extensive smooth terrain deposits outside of Imhotep (El-Maarry et al., 2015; Thomas et al., 2018). Its position on the nucleus and basin-like morphology make it an effective trap for incoming particles. Our model reproduces this observation, predicting substantial deposition at 0.5 m s^{-1} (Fig. 7C). Additional sediment inputs come from Atum up-slope at lower ejection velocities (Fig. 7B).

Atum is a terraced, fractured terrain with only a sparse smooth terrain mantling (El-Maarry et al., 2015; Thomas et al., 2018). While our model shows that Atum intercepts a modest number of particles at 0.5 m s^{-1} (Fig. 7C), most of this region acts as ejectors at higher velocities owing to Atum's large radial distance from the nucleus center (Fig. 7D). This dual role explains the observations—interception at low and moderate speeds contributes to thin, local accumulations, but persistent ejector behavior at >0.5 m s^{-1} prevents any substantial mantling from ever forming.

Serqet, located along the western edge of the small lobe, exhibits a mix of smooth mantling within depressions and ridges (El-Maarry et al., 2015; Thomas et al., 2018). At an ejection velocity of 0.5 m s^{-1}, our simulations predict maximum accumulation within the observed dust-covered smooth plain (Fig. 8B). At higher velocities, however, ejector facets emerge along the bounding ridges that frame this plain, leading to loss of sediment (Fig. 8D). This pattern matches the observed the coexistence of smooth deposits in the central Serqet basin with the cliff exposures to the north and the more rugged, boulder-strewn Nut region to the south.

Bastet, located on the eastern margin of the small lobe, is dominated by layered and fractured, consolidated material with only isolated smooth deposits (Thomas et al., 2018). Like Atum and western Imhotep/Khepry, Bastet sweeps up large numbers of particles at 0.5 m s^{-1}, but most facets transition to ejectors at higher speeds (Fig. 9). The scarcity of smooth terrain mantling here is consistent with our model—intercepted particles are not stable, and only small, low-velocity local transport can explain the thin, local accumulations observed.

Taken together, our results indicate that Anubis and Serqet serve as stable long-term repositories of smooth terrain sediment. Meanwhile, the promontories Atum and Bastet represent transient interception zones that readily eject material to the coma at higher velocities. This prevents any buildup of a thick, smooth terrain mantling, leaving only patchy smooth terrain deposits that match observations.

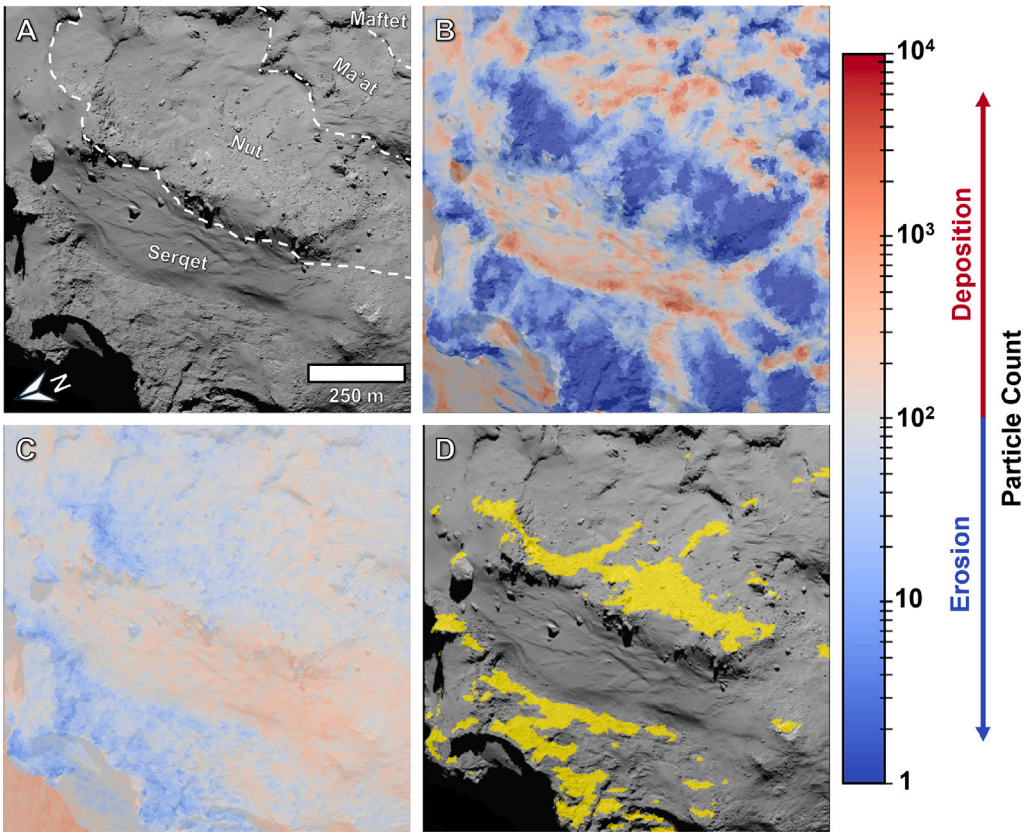

Fig. 8. Sediment redistribution in the Serqet region. (A) OSIRIS NAC image showing the Serqet smooth plain and surrounding terrains on the western edge of the small lobe, including the adjacent Nut, Ma'at, and Maftet regions. (B) Sediment redistribution at low ejection velocity (0.1 $m\,s^{-1}$, after 10 hops). At these speeds, sediment motion is highly localized—particles drain from the surrounding ridges and accumulate within topographic depressions across all regions. (C) Sediment redistribution at intermediate ejection velocity (0.5 $m\,s^{-1}$, after 10 hops). The smooth plain emerges as a major accumulation zone, consistent with the observed dust-covered surface (El-Maarry et al., 2015), while the bounding ridges begin to lose material. (D) At higher velocities (0.7 $m\,s^{-1}$), several of these bounding ridges transition into "ejectors" (highlighted in yellow), explaining the limited extent of mantling on the northern cliffs and the rugged, boulder-covered Nut region to the south. Together, these panels show that Serqet's patchy mantling and consolidated ridges arise naturally from localized accumulation at moderate velocities and ejector behavior at higher velocities.

3.3. Ash and Ma'at

The tops of both lobes — Ash on the large lobe and Ma'at on the small — largely consist of smooth terrain deposits. However, unlike Hapi, Imhotep, and Anubis, these deposits are comparatively thin, allowing the long-wavelength topography of the underlying bedrock to remain visible (Birch et al., 2017; El-Maarry et al., 2019).

At ejection velocities of 0.5 $m\,s^{-1}$, our simulations predict little to no net deposition across the low-slope plains of these regions, while steeper slopes (e.g., cliffs and associated talus) experience net sediment loss (Fig. 5, +Z). Crucially, both Ash and Ma'at are dynamically isolated within the global transport network—very few trajectories are capable of delivering material to the tops of either lobe (Figs. A.10, A.11). Sediment mobilized at 0.5 $m\,s^{-1}$ is either re-deposited locally or transported into adjacent basins, primarily Hapi. At lower ejection velocities, motion becomes even more localized: material is simply cleared off cliffs and accumulates at their base (Fig. 4, +Z).

Although our main analysis focuses on the 0.5 $m\,s^{-1}$ regime, higher ejection velocities (0.6–0.9 $m\,s^{-1}$) introduce an important transition. At these speeds, Ash and Ma'at are no longer fully isolated and begin to intercept modest amounts of sediment (Figs. C.21–C.24), predominantly sourced from Hapi, consistent with previous ballistic modeling (Thomas et al., 2015a). Particles capable of reaching the lobe tops at such high speeds are expected to be relatively small (Skorov et al., 2016) and volatile-depleted due to their long flight times (Davidsson et al., 2021). As a result, their deposition in Ash and Ma'at would further suppress any activity in the region.

Taken together — the deposition of a volatile-poor surface layer at high velocities, combined with both the lack of delivery of new sediment at lower velocities and the limited removal of material except at the lowest velocities — our simulations closely reproduce Rosetta observations. Systematic searches revealed no large-scale surface changes in either region (Barrington et al., 2023), barring minor mass-wasting events (Bouquety et al., 2021). Similarly, independent modeling of ROSINA data and non-gravitational accelerations reproduces 67P's global activity without requiring any significant outgassing from Ash or Ma'at (Marschall et al., 2016; Kramer et al., 2019; Attree et al., 2023). Consequently, these lobe tops appear largely dormant, shaped by weak reworking of a thin, volatile-depleted sediment layer that is minimally replenished with fresh, volatile-rich material.

3.4. Hapi, Seth, and Hathor

Hapi, like Imhotep, is a broad smooth-terrain deposit situated within a major gravitational low. Blanketing the north pole, it is bounded by the vertical Hathor cliffs and the smooth terrain-covered terraces of Seth (El-Maarry et al., 2015). Hapi is illuminated primarily at large heliocentric distances and transitions into polar winter near perihelion. In the lead up to perihelion, Hapi was highly active as both a large source of dust (Sierks et al., 2015) and rich with small-scale migrating scarps (El-Maarry et al., 2017; Birch et al., 2019; Davidsson et al., 2022; Barrington et al., 2023).

Hapi, Seth, and Hathor, all act as major accumulation zones at 0.5 $m\,s^{-1}$ in our simulations (Fig. 5, +Z), with most of the sediment

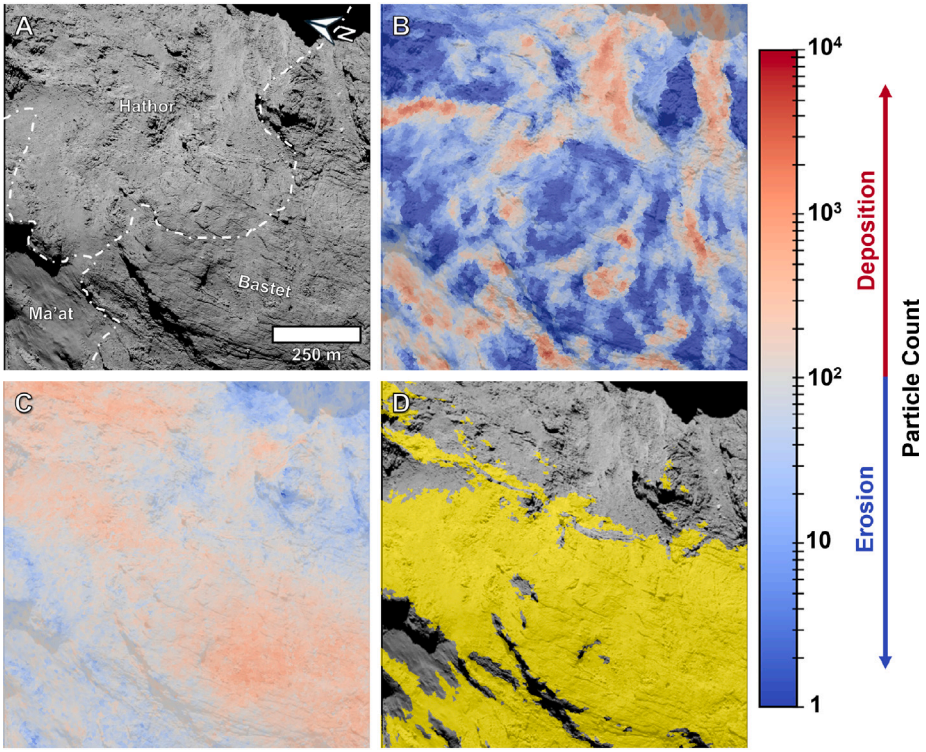

Fig. 9. Sediment redistribution in the Bastet region. (A) OSIRIS NAC image showing the fractured, consolidated terrains within the Bastet region on the eastern edge of the small lobe, including the adjacent Hathor and Ma'at regions. (B) Sediment redistribution at low ejection velocity (0.1 m s^{-1}, after 10 hops). At these speeds, sediment clears off cliffs into the flatter basins . (C) Sediment redistribution at intermediate ejection velocity (0.5 m s^{-1}, after 10 hops). The consolidated, fractured terrains of Bastet and the consolidated regions of Hathor are both predicted to accumulate sediment, contrary to observations. (D) At higher velocities (0.7 m s^{-1}), large portions of Bastet and parts of Hathor transition into "ejectors" (highlighted in yellow). Thus, the sediment that is predicted to accumulate here at 0.5 m s^{-1} is likely lost by higher velocity ejections. Together, our results show that the lack of smooth deposits in Bastet despite localized accumulation at moderate velocities can be explained by the persistence of ejectors at higher velocities.

sourced locally or from Aten, Ash, and Ma'at (Figs. A.12, A.13, A.14). However, contributions from Ash and Ma'at are likely overestimated since both are weakly active, as discussed above. Sediment ejected from Seth and Hathor primarily settles in Hapi. In addition, much of the sediment that accumulates on the steep slopes of these regions in our simulations would, in reality, flow downslope into Hapi—a process not captured in our model. At lower ejection velocities, sediment similarly clears from the steep slopes of Seth and Hathor and collects at their base (Fig. 4, +Z). Finally, sediment struggles to escape Hapi except at the highest velocities, as the steep topography surrounding the basin acts as an efficient trap, consistent with previous models (Thomas et al., 2015a). This feedback reinforces Hapi's role as the dominant depositional basin in the northern hemisphere.

Rosetta observations reveal only limited evidence for sediment accumulation in Hapi. Birch et al. (2019) only observed erosion, and topographic measurements from Cambianica et al. (2020) show no conclusive changes. This mismatch, however, can be attributed to the temporal averaging of our ejection probability calculations (Section 2), which integrate sediment transport fluxes across the comet's full orbit. Instead, we hypothesize that Hapi is indeed replenished by Hathor and Seth, but through thermal shock fracturing of Hathor at aphelion, outside the period of the Rosetta mission. Observations of 67P at aphelion would therefore see the crumbling of the Hathor cliff and the deposition of new sediment in Hapi. If so, such smooth terrain sediment would differ from the finer dust that mantles other deposits, instead consisting of chunkier, more ice-rich material. Such ice-rich sediment is consistent with Hapi's role as the primary source of water vapor from the northern hemisphere during the inbound leg of Rosetta's escort, even though it did not receive the highest solar flux at these latitudes (Fougere et al., 2016).

3.5. Southern hemisphere regions

The southern hemisphere of 67P stands in marked contrast to the north, dominated by fractured, consolidated terrains and largely devoid of extensive smooth terrain deposits (Birch et al., 2017; El-Maarry et al., 2019). Smooth terrains occur only in isolated patches, typically within sheltered alcoves or as thin veneers draped over the underlying bedrock (El-Maarry et al., 2016).

At 0.5 m s^{-1}, our simulations predict significant erosion across most of the southern terrains (Fig. 5, -Z). However, modest deposition is predicted across parts of Anhur, Geb, Neith, Sobek, and Wosret, in contrast to observations. The modeled deposits arise primarily from local transport: most of the sediment delivered to these regions originates from nearby facets rather than from global redistribution (Fig. A.15). Consequently, sediment delivery coincides with the same orbital phases when activity — and thus erosion — is at its peak. In reality, these periods of intense activity produce strong gas fluxes that would prevent fallback and re-accumulation, and instead expel material toward more stable regions in the north (Marschall et al., 2020). Because our model does not account for gas drag, this suppression of fallback is not captured, leading to an overestimate of sediment retention in the southern terrains.

4. Discussion

Rosetta's observations of 67P established ballistic transport as a major sediment transport mechanism for cometary surfaces. Early work by Thomas et al. (2015a) showed that particles launched from the Hapi region in the neck over a range of sub-escape velocities can be redeposited in northern terrains such as Ash, Ma'at, and Babi. This

work demonstrated that airfall is a plausible mechanism for forming smooth deposits. Lai et al. (2016) extended this picture to the scale of the entire nucleus by coupling dust transport to seasonally varying outgassing, showing that particles are preferentially redistributed from south to north and that this process can help explain the comet's large-scale hemispheric dichotomy. These studies established the importance of hemispheric-scale erosion and redistribution, but did not resolve the local-scale diversity of terrain morphologies observed across the nucleus.

More recently, Kloos et al. (2025) advanced this framework by coupling three-dimensional ballistic sediment transport to a thermophysical model that tracks both sublimation-driven erosion and the accumulation of fallback material through time. In their model, dust emission rates are directly calculated from local sublimation rates across discrete orbital epochs, assuming spatially uniform surface properties and a prescribed volatile inventory (through a fixed dust–ice ratio). Particle launch speeds are then randomly sampled from a uniform distribution spanning 0.1–1 $m\,s^{-1}$. Within this framework, Kloos et al. (2025) demonstrate that nucleus shape and rotation generate spatially heterogeneous fallback patterns and persistent depositional sinks, consistent with several large-scale trends observed by Rosetta, including enhanced deposition along the leading edges of both lobes. However, because their redistribution patterns reflect the combined effects of transport operating across a broad range of launch velocities, they effectively convolve multiple distinct transport pathways into a single aggregate result. While this approach is valuable for assessing net mass balance, the superposition of different kinematic regimes masks the specific topographic "filters" that define individual terrain boundaries. Consequently, such aggregate models still struggle to reproduce the full diversity of local surface morphologies and specific activity patterns recorded by Rosetta.

A central challenge for any such quantitative sediment transport model is that several key aspects of cometary activity remain unconstrained. The microphysics governing erosion and particle ejection are still not well understood (Kührt and Keller, 1994; Jewitt et al., 2019; Vincent et al., 2019). Critical uncertainties persist regarding the structure and composition of near-surface dust–ice mixtures (Choukroun et al., 2020), how thermal cycling mobilizes them, what particle sizes can be lofted at a given gas flux (Fulle et al., 2019; Gundlach et al., 2020; Bischoff et al., 2023; Attree et al., 2024, 2025; Schuckart and Blum, 2025), and how much ice they retain during ballistic transport (Davidsson et al., 2021). Quantitative predictions of sediment redistribution therefore necessarily depend on assumptions about poorly constrained source physics. To limit the influence of those assumptions on our interpretations, we deliberately adopt an approach such that we focus only on the post-launch transport problem, using orbit-integrated erosion estimates only to weight the relative likelihood of ejection across the surface. In this way, we explore a controlled set of launch velocities to determine what sets the global distribution of dust deposits across 67P, and any local-scale variability. We aimed to do so semi-qualitatively such that we do not impose a specific particle-size distribution or launch-velocity prescription.

Accordingly, starting from a uniform sediment distribution and constraining each facet's ability to launch material using orbitally averaged erosion estimates (Section 2), we resolve sediment motion into discrete velocity regimes and then follow each regime through successive cycles of ballistic transport until the redistribution patterns converge. This approach allows the transport pathways associated with each launch speed to be examined independently, rather than combining all launch speeds into a single aggregate redistribution pattern. As shown in Section 3, different launch speeds produce fundamentally different styles of sediment redistribution, ranging from localized hopping and basin-confined accumulation to long-range transfer and eventual loss from discrete locations on the nucleus. By isolating these regimes, we identify three fundamental terrain types — (i) collectors, (ii) shadow zones, and (iii) ejectors — that together govern how sediment is redistributed across the surface over long timescales.

Viewed through our new velocity-resolved framework, we are able to then qualitatively explain not only the broad distribution of dust deposits on 67P, but also specific local-scale observations that are more difficult to capture in aggregate models. These include sharp transitions from smooth to rough terrain within the same topographic boundary, as well as the absence of significant sediment accumulation in extensive portions of the leading edges of the nucleus, such as Bastet, which might otherwise be expected to favor deposition (Kloos et al., 2025). This success suggests that, while microphysical processes such as specific particle-size distributions, dust–ice ratios, or volatile-driven ejection mechanisms are critical for understanding short-term variability and the internal composition of deposits, they are secondary to the structural controls governing the nucleus's long-term evolution. By isolating transport into discrete velocity bins, we show that the large-scale organization of 67P's surface is controlled by two linked processes. The thermophysical state of the nucleus influences where particles are preferentially mobilized, how many particles are mobilized, and how often mobilization takes place. Meanwhile, the comet's topography, gravity, and rotation govern how those particles are redistributed across the surface. In other words, the many unknown physical parameters and mechanisms affect the rates of sediment transport, but do not appear to affect where material is transported, which is instead controlled by the comet's seasonal insolation geometry and first-order shape.

With future improvements in our understanding of ejection physics, these velocity-specific pathways can be integrated into fully quantitative, time-resolved models to reconcile the full suite of Rosetta's diverse temporal observations. In particular, as thermophysical models become better able to predict local production rates and those production rates can be translated into particle-size-dependent launch-velocity distributions, our facet-to-facet transport maps provide a physically grounded and computationally efficient way to track the subsequent motion of sediment across the nucleus. Because these transport pathways are determined primarily by the shape, gravity field, and rotation of the nucleus, they should remain more robust to assumptions about the poorly constrained microphysical properties of the comet, except for the smallest particles whose trajectories are more strongly modified by gas drag. Coupled with a framework such as that developed by Kloos et al. (2025), in which the thermophysical model incorporates both erosion and fallback into the evolving dust mantle, our simulation results could be used as look-up tables that enable quantitative predictions of where sediment is produced, how much is redistributed or lost, and which regions remain sufficiently quiescent to retain mantling. Such a framework would also be well positioned to test specific geomorphic hypotheses, such as whether cryogenic thermal cycles at aphelion drive mass wasting from the massive cliffs of Hathor and Seth and thereby nourish the Hapi deposits. Ultimately, future missions such as CAESAR (Squyres et al., 2018), which may revisit 67P near aphelion, could provide critical ground truth by determining whether Hapi indeed accumulates new mantling at this time and whether Ash and Ma'at remain morphologically stable and volatile depleted.

Finally, the perspective offered by our analysis re-frames cometary landscapes as self-organizing sedimentary systems, in which repeated ballistic transport redistributes material along persistent routes imposed by the large-scale topography. In this sense, cometary surface evolution is analogous to fluvial, aeolian, and glacial systems on Earth, where landscapes route sediment along predictable pathways set by their own relief (Perron et al., 2008; Dietrich et al., 2013). Although this coupling on comets occurs in a fundamentally different environment — defined by microgravity and vacuum, with sediment motion occurring above the surface rather than across it — the governing principle remains the same. Topographic relief and ballistic dynamics interact to produce coherent, predictable patterns that dictate the long-term character of the surface. By revealing how these processes

combine to shape 67P, our work provides a unified geomorphic framework that can be applied to the broader population of cometary nuclei, enabling quantitative predictions of surface evolution and guiding the exploration of these primitive bodies.

CRediT authorship contribution statement

Abhinav S. Jindal: Writing – review & editing, Writing – original draft, Visualization, Validation, Software, Project administration, Methodology, Investigation, Funding acquisition, Formal analysis, Data curation, Conceptualization. **Raphael Marschall:** Writing – review & editing, Validation, Software, Resources, Methodology, Investigation, Formal analysis, Data curation, Conceptualization. **Nicholas Attree:** Writing – review & editing, Validation, Resources, Methodology, Funding acquisition, Conceptualization. **Jason M. Soderblom:** Writing – review & editing, Funding acquisition, Conceptualization. **Björn J.R. Davidsson:** Writing – review & editing, Conceptualization. **Jean-Baptiste Vincent:** Writing – review & editing, Conceptualization. **Olivier Groussin:** Writing – review & editing, Conceptualization. **Orkan M. Umurhan:** Writing – review & editing, Funding acquisition, Conceptualization. **Jordan K. Steckloff:** Writing – review & editing, Funding acquisition, Conceptualization. **Samuel P.D. Birch:** Writing – review & editing, Writing – original draft, Visualization, Validation, Supervision, Resources, Project administration, Methodology, Investigation, Funding acquisition, Conceptualization.

Declaration of competing interest

The authors declare that they have no known competing financial interests or personal relationships that could have appeared to influence the work reported in this paper.

Acknowledgments

We thank the Observatoire de la Côte d'Azur for hosting A.S.J., R.M., N.A., and S.P.D.B. for a collaborative visit that enabled synthesis of our results and completion of this work. Parts of this research was carried out at the Jet Propulsion Laboratory, California Institute of Technology, under a contract with the National Aeronautics and Space Administration. A.S.J. and S.P.D.B. were supported by the NASA Discovery Data Analysis Program (grants: 80NSSC24K0060 and 80NSSC25K0030). S.P.D.B. would also like to acknowledge the Heising-Simons Foundation, United States for support (51 Pegasi b Fellowship). J.K.S. was supported by NASA, United States (grants: 80NSSC19K1313 and 80NSSC22K1399). N.A. acknowledges financial support from project PID2021-126365NB-C21 (MCI/AEI/FEDER, UE) and from the Severo Ochoa grant CEX2021-001131-S funded by MCI/AEI/10.13039/501100011033. This work was also supported by the International Space Science Institute (ISSI) in Bern, through ISSI International Team project #547 (Understanding the Activity of Comets Through 67P's Dynamics).

Appendix A. Identification of sediment source regions

Figs. A.10–A.15 show the source regions contributing sediment to selected target areas (highlighted in green) at an ejection velocity of 0.5 $\mathrm{m\,s^{-1}}$. These figures are intended to visualize the directional structure of the ballistic transport network and to identify which surface facets are capable of supplying material to a given region under moderate ejection velocities.

Each figure presents views along the six principal axes of the nucleus. Colored facets represent source regions from which at least one simulated particle successfully reaches the target area within the multi-hop transport framework. Facets that do not contribute any sediment to the selected target are left uncolored.

Source regions are shaded by their source contribution fraction, defined as

$$f_{source} = \frac{N_{target}}{N_{ejected}}, \tag{A.1}$$

where N_{target} is the number of particles ejected from a given source facet that ultimately reach the target region, and $N_{ejected}$ is the total number of particles launched from that facet at the specified ejection velocity. This quantity isolates the geometric efficiency of sediment transfer between source and target regions and depends only on the ballistic transport pathways determined by the comet's shape, gravity, and rotation.

The source contribution fraction does not represent the absolute sediment flux delivered to the target. The actual mass transferred from a given source region additionally depends on the local ejection probability and the availability of sediment for mobilization, which

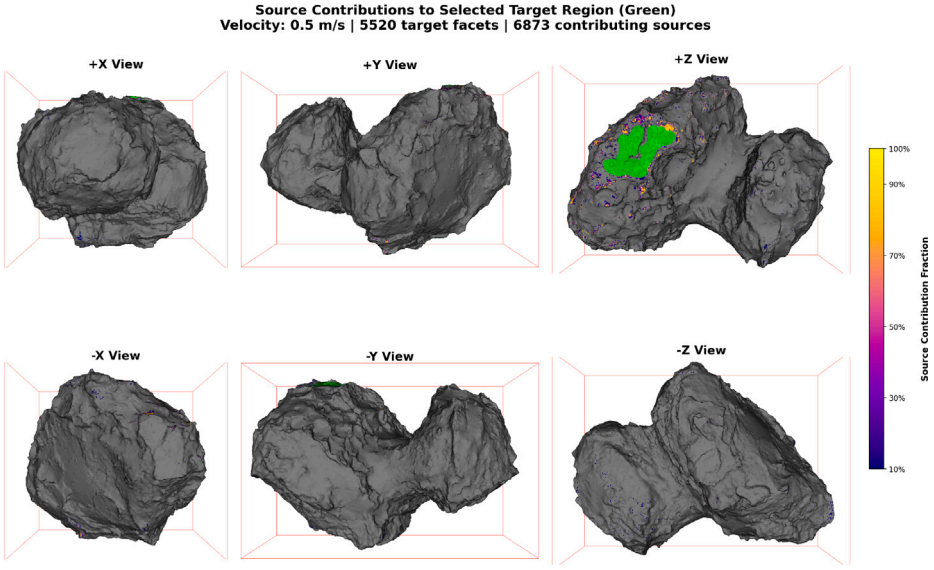

Fig. A.10. Sources of sediment for Ash (green). Colored facets indicate source regions capable of delivering sediment to Ash at an ejection velocity of 0.5 $\mathrm{m\,s^{-1}}$ and are shaded by their source contribution fraction. See Appendix A for a full description of the interpretation.

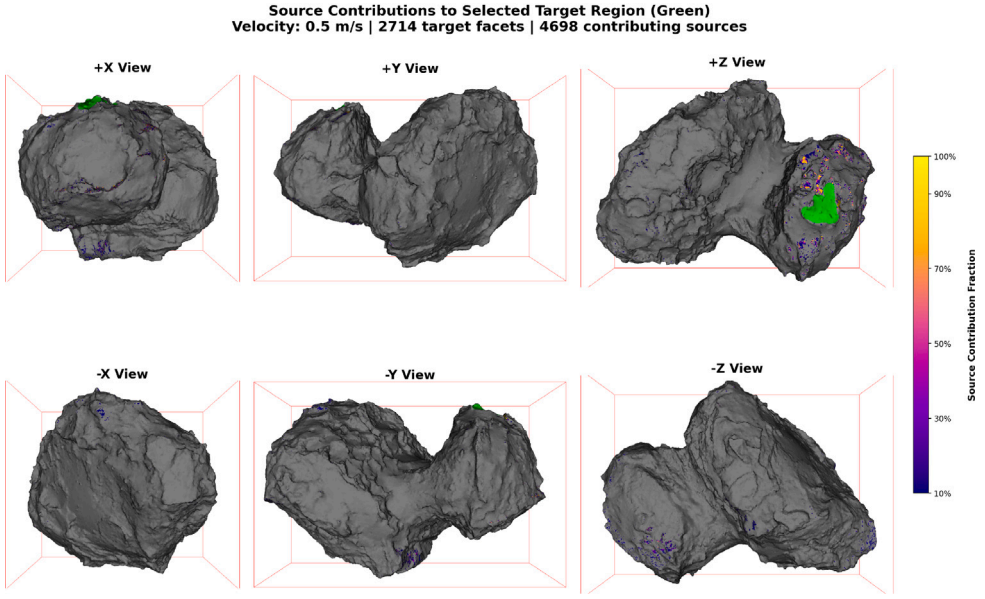

Fig. A.11. Sources of sediment for Ma'at (green). Colored facets indicate source regions capable of delivering sediment to Ma'at at an ejection velocity of 0.5 $m\,s^{-1}$ and are shaded by their source contribution fraction. See Appendix A for a full description of the interpretation.

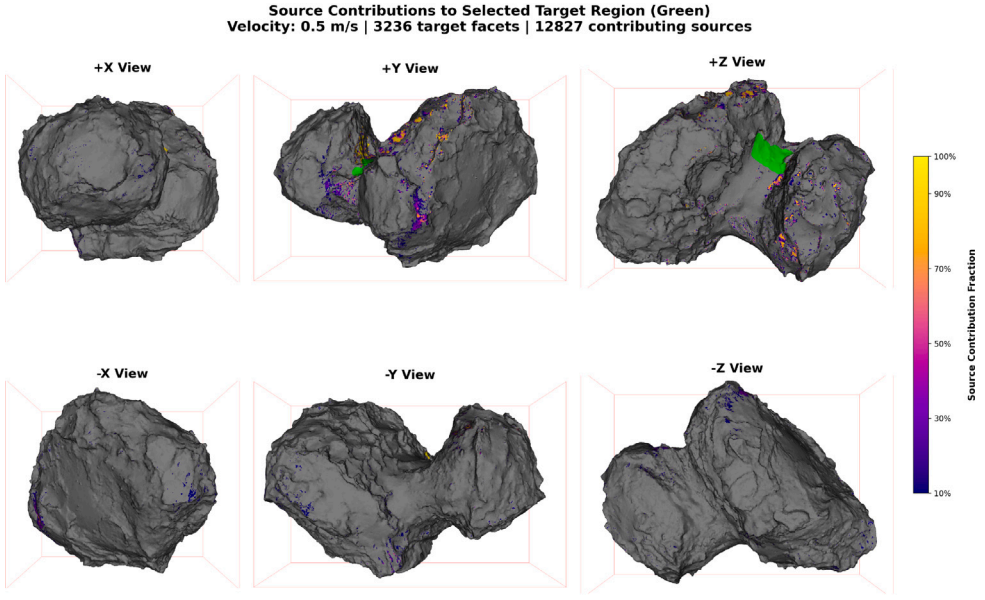

Fig. A.12. Sources of sediment for the eastern portion of Hapi (green). Colored facets indicate source regions capable of delivering sediment to the eastern portion of Hapi at an ejection velocity of 0.5 $m\,s^{-1}$ and are shaded by their source contribution fraction. See Appendix A for a full description of the interpretation.

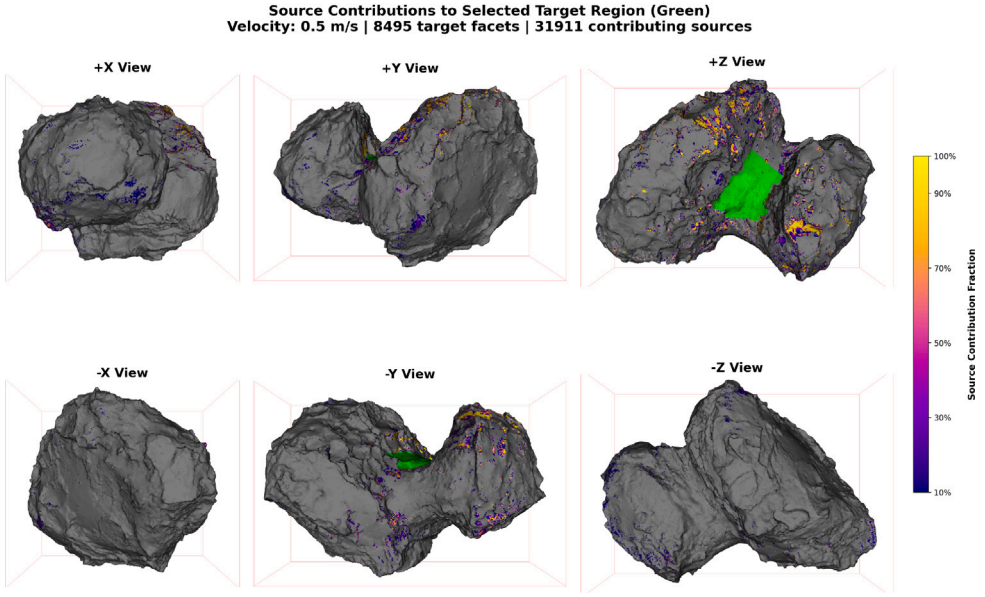

Fig. A.13. Sources of sediment for the central portion of Hapi (green). Colored facets indicate source regions capable of delivering sediment to the central portion of Hapi at an ejection velocity of 0.5 $m\,s^{-1}$ and are shaded by their source contribution fraction. See Appendix A for a full description of the interpretation.

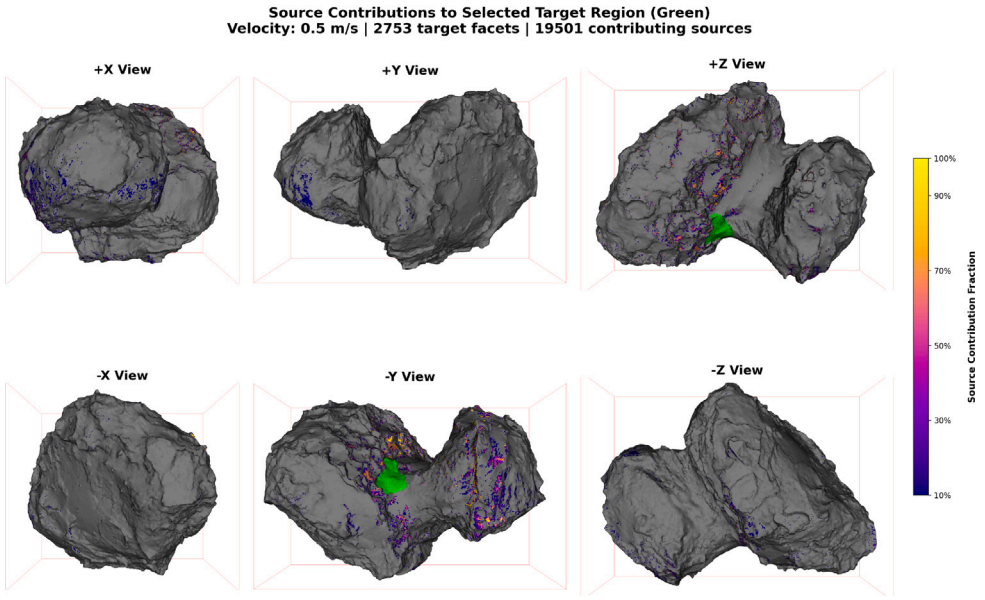

Fig. A.14. Sources of sediment for the Western portion of Hapi (green) Colored facets indicate source regions capable of delivering sediment to the western portion of Hapi at an ejection velocity of 0.5 $m\,s^{-1}$ and are shaded by their source contribution fraction. See Appendix A for a full description of the interpretation. (For interpretation of the references to color in this figure legend, the reader is referred to the web version of this article.)

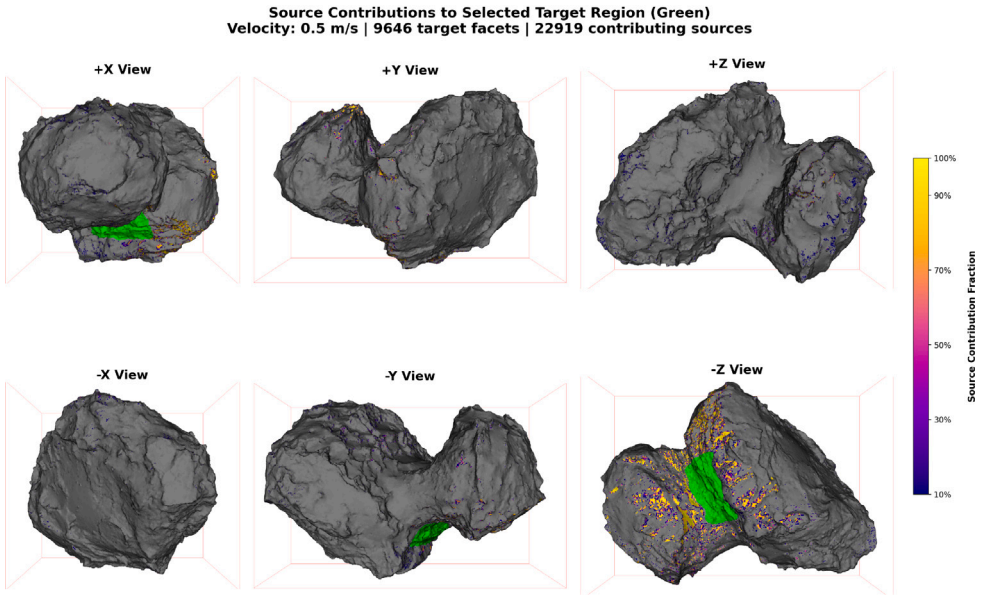

Fig. A.15. Sources of sediment for the Southern Terrains(green) Colored facets indicate source regions capable of delivering sediment to the southern terrains at an ejection velocity of 0.5 $m\,s^{-1}$ and are shaded by their source contribution fraction. See Appendix A for a full description of the interpretation. (For interpretation of the references to color in this figure legend, the reader is referred to the web version of this article.)

vary spatially and are treated separately in the main simulations. Consequently, facets with high source contribution fractions may still deliver little material if their local ejection probability is low, while facets with lower geometric efficiency may dominate the net flux if they are highly active.

All source–target relationships shown here are computed for a fixed ejection velocity of 0.5 $m\,s^{-1}$, corresponding to the regime in which sediment transport becomes global and strongly influenced by the nucleus-scale transport network. At lower velocities, source regions are more localized, while at higher velocities ejector facets increasingly dominate the transport behavior (see 3 and Appendix C).

The Python code used to compute and visualize source contribution fractions for arbitrary target regions is publicly available via a Zenodo repository (Jindal, 2025a) (https://doi.org/10.5281/zenodo.17574889). This code allows users to select any region of interest on the shape model and generate the corresponding source maps, facilitating direct comparison with additional morphologic units or alternative transport scenarios.

Appendix B. List of images used in study

Table B.1 lists all Rosetta images used for visual comparison with the results of our ballistic sediment transport simulations. All OSIRIS and Philae images listed below are publicly available through the ESA Planetary Science Archive.

Table B.1
Image IDs used in figures. All images are available to download on the ESA Planetary Science Archive.

Image ID	Figure
N20160815T161736438ID4EF22	Fig. 1A
Philae CIVA mosaic from Bibring et al. (2015) Fig. S9	Fig. 1B
N20160812T121734755ID4EF22	Fig. 1C
ROL_FS2_141112153336_336_04	Fig. 1D
N20160813T005736588ID4EF24	Fig. 1E
N20160911T235733878ID4EF22	Fig. 1F
N20140903T034422640ID4EF22	Fig. 6
N20160610T041253713ID4EF22	Fig. 7
N20160616T001202935ID4EF22	Fig. 8
N20160615T081537509ID4EF22	Fig. 9

Appendix C. Ballistic sediment transport movies

This appendix accompanies the supplementary movies (Appendix D), which visualize multi-hop ballistic sediment redistribution on comet 67P for fixed ejection velocities between 0.1 and 0.9 $m\,s^{-1}$. Each movie shows the evolution of sediment transport at a single launch speed, illustrating how redistribution pathways change systematically with velocity.

At lower ejection velocities (0.1–0.5 $m\,s^{-1}$; Figs. C.16–C.20), sediment is largely redistributed without significant loss to space. At the lowest velocities, particles are trapped within local topographic basins, whereas with increasing velocity their motion becomes progressively influenced by the nucleus's large-scale shape and rotation. In this regime, redistribution proceeds gradually toward a stable configuration dominated by persistent depositional sinks.

At higher velocities (0.6–0.9 $m\,s^{-1}$; Figs. C.21–C.24), sediment transport becomes increasingly dominated by escape from the nucleus. As described in Section 2.1, facets whose launch trajectories exceed the adopted Hill-sphere cut-off at a given velocity are treated as incapable of ejecting particles and are therefore initialized with zero available sediment. These facets correspond to regions from which any sediment reaching them would, in reality, be rapidly ejected to space.

As the simulations progress, sediment delivered from elsewhere on the nucleus is numerically retained on these facets, producing an apparent increase in particle abundance. This accumulation should not be interpreted as stable surface deposition. Instead, these regions act as effective ejectors: over many hops, sediment from across the nucleus is progressively funneled toward these facets and removed from the system. Consequently, at high ejection velocities, the dominant outcome of ballistic transport is widespread mass loss rather than long-term surface retention.

The supplementary movies thus illustrate a fundamental transition in sediment behavior with increasing launch speed—from surface-confined redistribution and organized accumulation at low velocities to ejector-dominated loss pathways at high velocities.

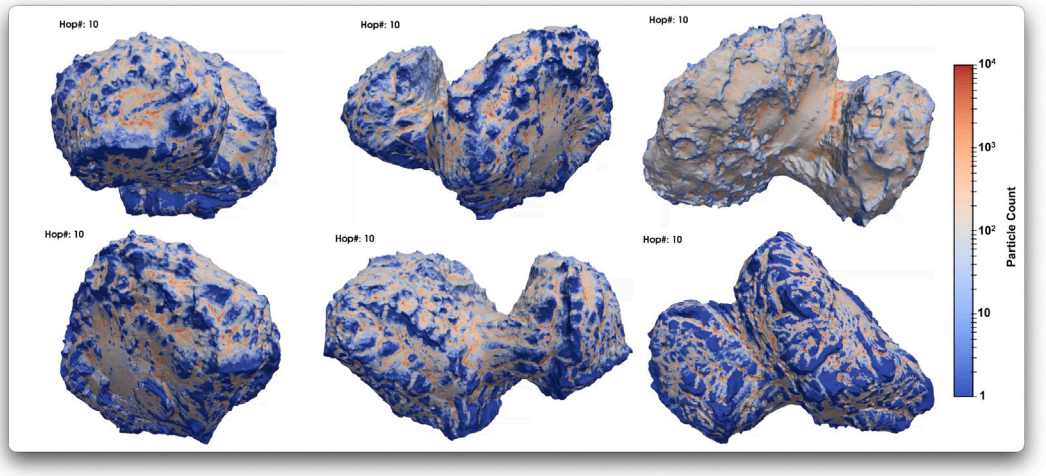

Fig. C.16. Sediment redistribution at 0.1 $m\,s^{-1}$. Sediment drains from steep slopes and accumulates in nearby topographic lows, becoming trapped after repeated hops. Refer to Appendix D, Video S1, to see the complete redistribution at this velocity.

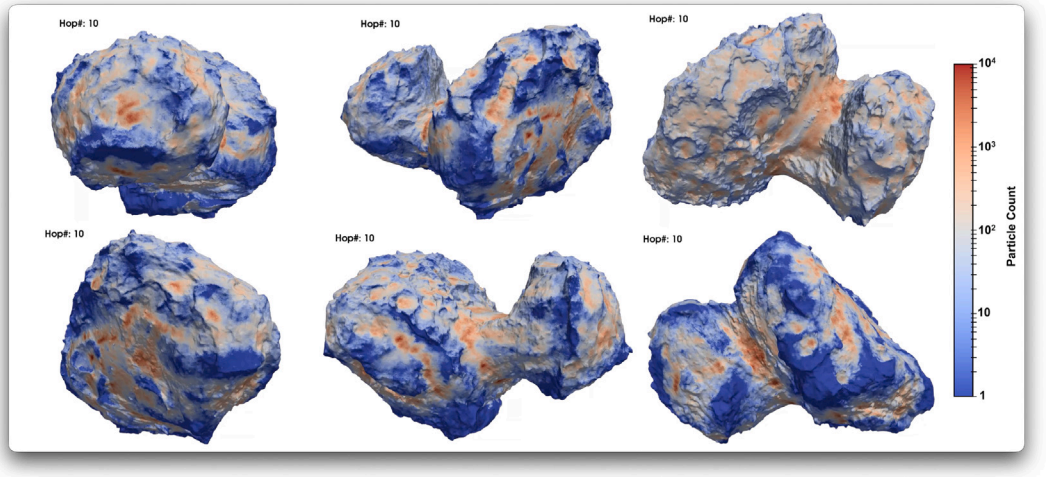

Fig. C.17. Sediment redistribution at 0.2 $m\,s^{-1}$. Sediment motion remains locally confined but occurs more efficiently than at 0.1 $m\,s^{-1}$, rapidly clearing slopes and filling adjacent basins. Refer to Appendix D, Video S2, to see the complete redistribution at this velocity.

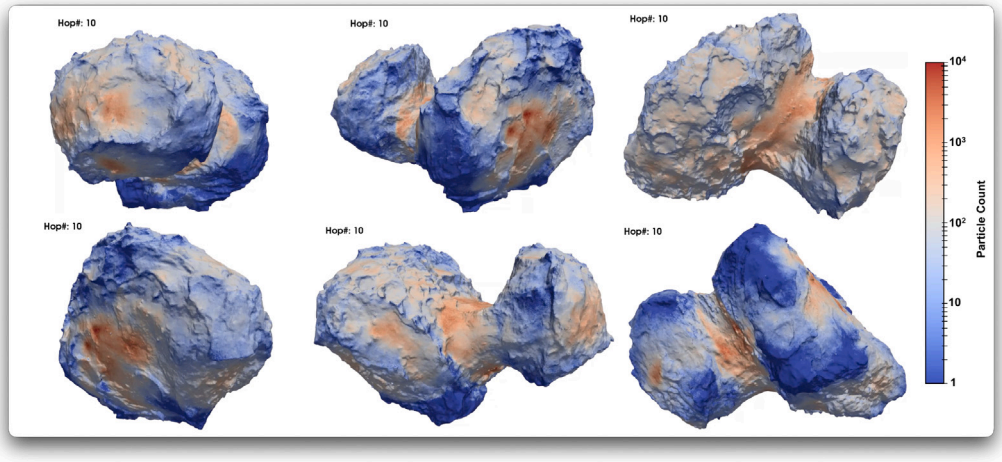

Fig. C.18. Sediment redistribution at 0.3 $m\,s^{-1}$. Sediment begins to move beyond local basins, gradually concentrating in global gravitational lows such as Hapi, Imhotep, and the southern neck region. The movie shows results through Hop#: 100; at this stage, some regions outside these basins still retain modest accumulations, but these progressively clear over time as material settles into the primary sinks. Refer to Appendix D, Video S3, to see the complete redistribution at this velocity.

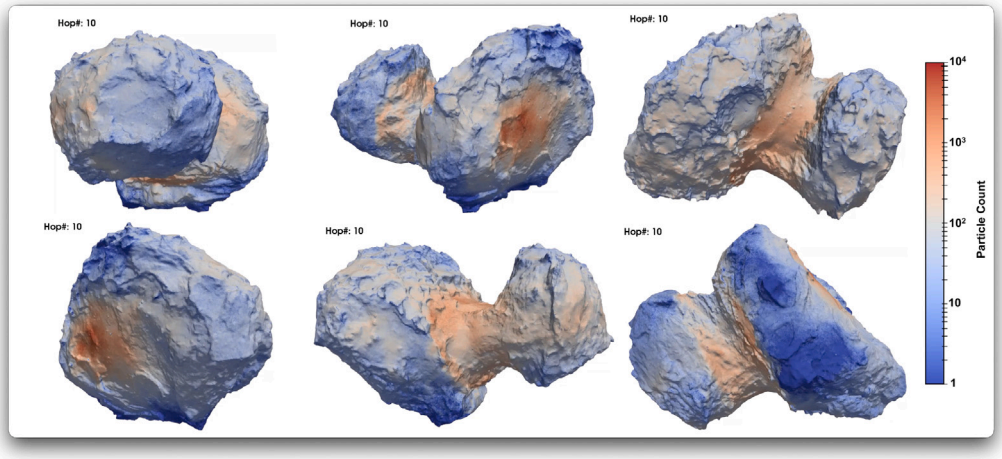

Fig. C.19. Sediment redistribution at 0.4 $m\,s^{-1}$. At 0.4 $m\,s^{-1}$, transport remains focused on global gravitational lows, though deposits within them appear more scattered than at 0.3 $m\,s^{-1}$, reflecting greater freedom of motion. Because the movie shows only the first 100 hops, redistribution is still ongoing: transient accumulations persist outside the main basins but would gradually dissipate as sediment continues to migrate toward the dominant sinks. Refer to Appendix D, Video S4, to see the complete redistribution at this velocity.

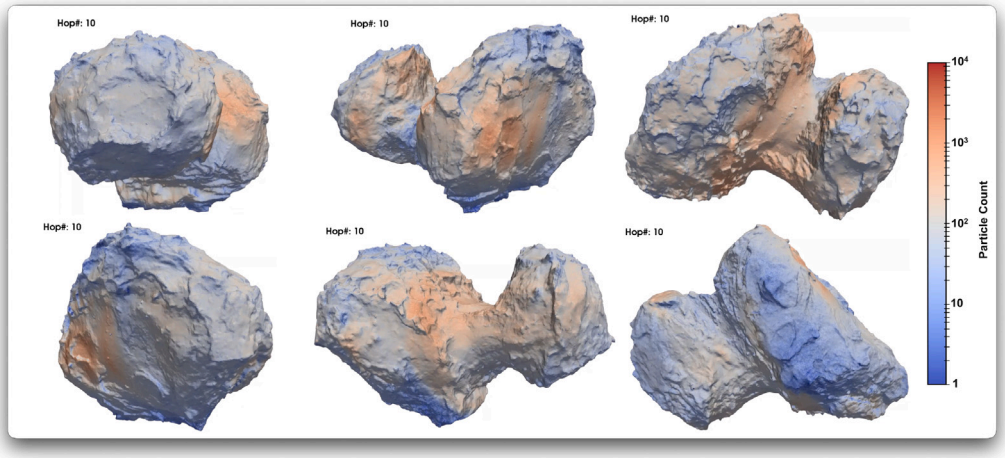

Fig. C.20. Sediment redistribution at 0.5 $m\,s^{-1}$. Sediment transport transitions from localized motion to near-global redistribution, strongly influenced by the comet's shape and rotation. Refer to Appendix D, Video S5, to see the complete redistribution at this velocity.

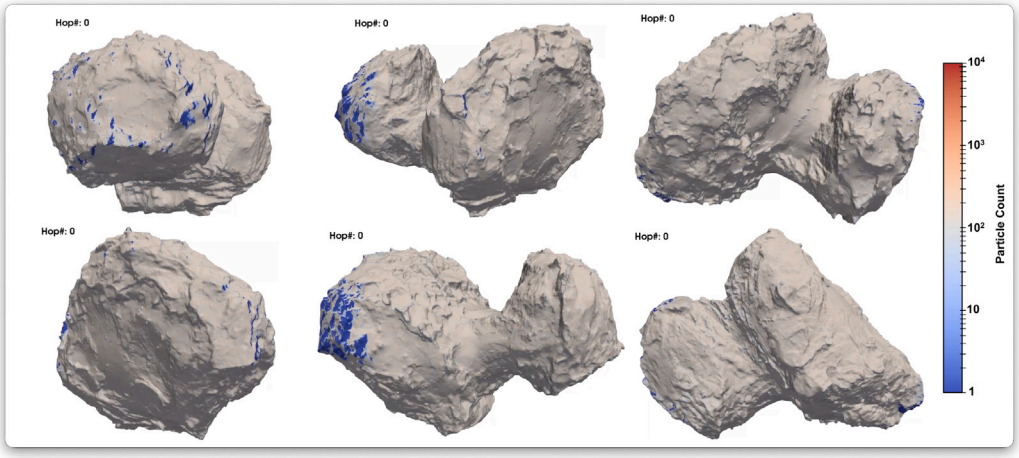

Fig. C.21. Sediment redistribution at 0.6 $m\,s^{-1}$. At 0.6 $m\,s^{-1}$, ejector facets become prominent for the first time, identifiable by the dark blue regions in the initial distribution (Hop#: 0) that start with no available sediment. Over time, these facets accumulate material delivered from elsewhere; however, in reality, any sediment deposited on such surfaces would be ejected to space and lost from the system (see Section 2). After 100 hops, these ejectors dominate the apparent accumulation pattern, while modest deposits persist in other regions that would continue to clear over longer timescales as material is funneled through the ejectors and ultimately lost. Refer to Appendix D, Video S6, to see the complete redistribution at this velocity.

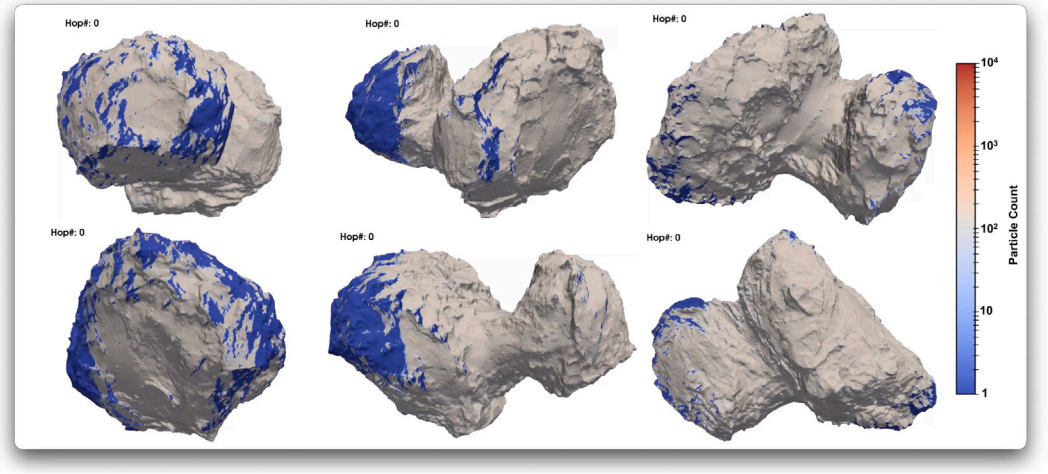

Fig. C.22. Sediment redistribution at 0.7 $\mathrm{m\,s^{-1}}$. Ejector facets dominate sediment behavior, following the same setup described for 0.6 $\mathrm{m\,s^{-1}}$ (Movie C.21). The fraction of ejectors increases, further reducing surface retention across the nucleus after 100 hops. Refer to Appendix D, Video S7, to see the complete redistribution at this velocity.

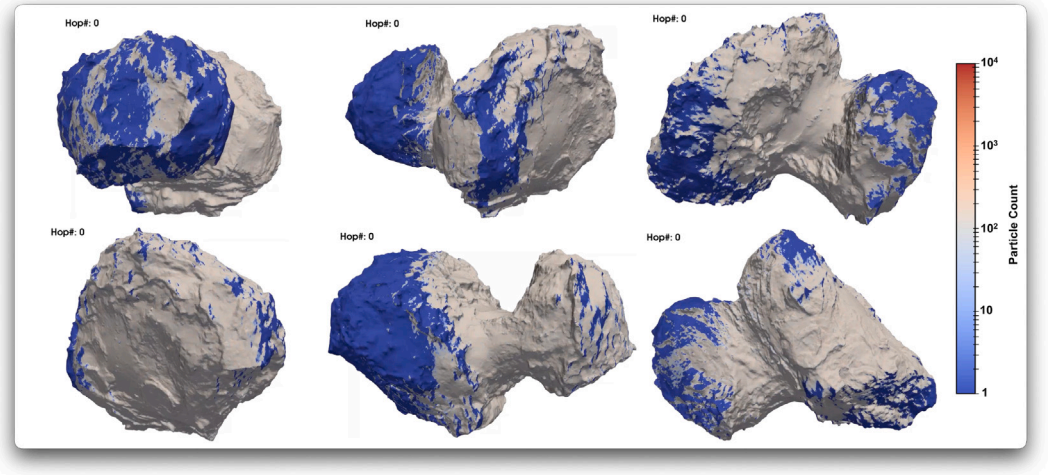

Fig. C.23. Sediment redistribution at 0.8 $\mathrm{m\,s^{-1}}$. Similar to 0.6 $\mathrm{m\,s^{-1}}$ (Movie C.21), but ejectors become even more widespread, leading to sparse surface accumulations as most trajectories result in escape. Refer to Appendix D, Video S8, to see the complete redistribution at this velocity.

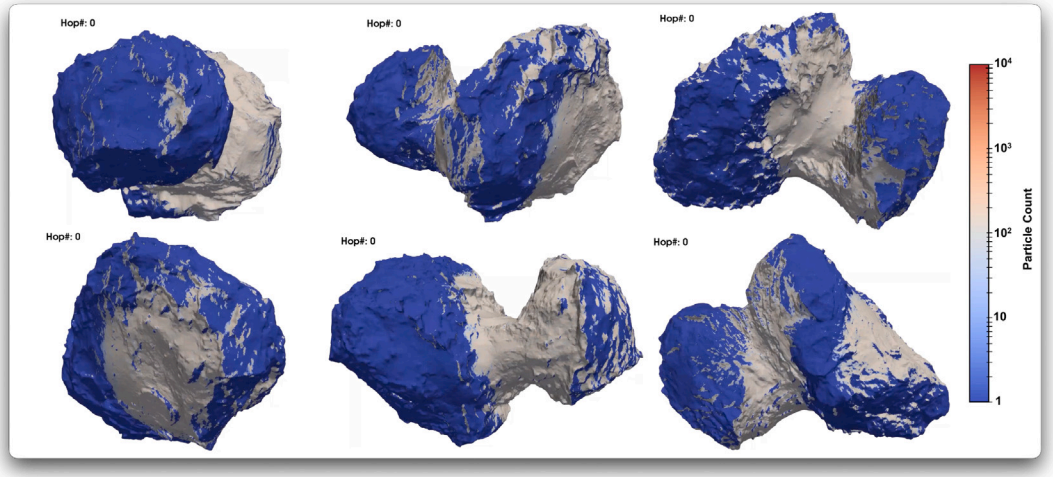

Fig. C.24. Sediment redistribution at 0.9 $\mathrm{m\,s^{-1}}$. At this velocity, ejectors encompass nearly the entire surface (see caption for Movie C.21 for setup). Surface retention is minimal, and most sediment is efficiently lost to space. Refer to Appendix D, Video S9, to see the complete redistribution at this velocity.

Appendix D. Supplementary data

Supplementary material related to this article can be found online at https://doi.org/10.1016/j.icarus.2026.117099.

Data availability

All Rosetta mission data used to create the figures are listed in Table B.1 and are publicly available via the ESA Planetary Science Archive (https://psa.esa.int/psa). The shape model, ejection probability maps, and analysis/processing scripts are archived in a Zenodo software repository (Jindal, 2025a), with source code also available on GitHub (https://github.com/abhinav-s-jindal/67P_sediment_transport_pathways). Pre-computed ballistic transport dictionaries (~5 GB) are archived in a separate Zenodo data repository (Jindal, 2025b). Visualization of results was performed using the open-source ParaView software (Ayachit, 2015). All materials are sufficient to reproduce the results and evaluate the conclusions presented in this paper.

References

Agarwal, J., A'Hearn, M.F., Vincent, J.B., Güttler, C., Höfner, S., Sierks, H., Tubiana, C., Barbieri, C., Lamy, P.L., Rodrigo, R., Koschny, D., Rickman, H., Barucci, M.A., Bertaux, J.L., Bertini, I., Boudreault, S., Cremonese, G., Da Deppo, V., Davidsson, B., Debei, S., De Cecco, M., Deller, J., Fornasier, S., Fulle, M., Gicquel, A., Groussin, O., Gutiérrez, P.J., Hofmann, M., Hviid, S.F., Ip, W.H., Jorda, L., Keller, H.U., Knollenberg, J., Kramm, J.R., Kührt, E., Küppers, M., Lara, L.M., Lazzarin, M., Lopez Moreno, J.J., Marzari, F., Naletto, G., Oklay, N., Shi, X., Thomas, N., 2016. Acceleration of individual, decimetre-sized aggregates in the lower coma of comet 67P/Churyumov–Gerasimenko. Mon. Not. R. Astron. Soc. 462, S78–S88. http://dx.doi.org/10.1093/mnras/stw2179.

A'Hearn, M.F., Belton, M.J.S., Delamere, W.A., Feaga, L.M., Hampton, D., Kissel, J., Klaasen, K.P., McFadden, L.A., Meech, K.J., Melosh, H.J., Schultz, P.H., Sunshine, J.M., Thomas, P.C., Veverka, J., Wellnitz, D.D., Yeomans, D.K., Besse, S., Bodewits, D., Bowling, T.J., Carcich, B.T., Collins, S.M., Farnham, T.L., Groussin, O., Hermalyn, B., Kelley, M.S., Kelley, M.S., Li, J.Y., Lindler, D.J., Lisse, C.M., McLaughlin, S.A., Merlin, F., Protopapa, S., Richardson, J.E., Williams, J.L., 2011. EPOXI at comet Hartley 2. Science 332, 1396–1400. http://dx.doi.org/10.1126/science.1204054.

A'Hearn, M.F., Belton, M.J.S., Delamere, W.A., Kissel, J., Klaasen, K.P., McFadden, L.A., Meech, K.J., Melosh, H.J., Schultz, P.H., Sunshine, J.M., Thomas, P.C., Veverka, J., Yeomans, D.K., Baca, M.W., Busko, I., Crockett, C.J., Collins, S.M., Desnoyer, M., Eberhardy, C.A., Ernst, C.M., Farnham, T.L., Feaga, L., Groussin, O., Hampton, D., Ipatov, S.I., Li, J.Y., Lindler, D., Lisse, C.M., Mastrodemos, N., Owen, W.M., Richardson, J.E., Wellnitz, D.D., White, R.L., 2005. Deep impact: Excavating comet tempel 1. Science 310, 258–264. http://dx.doi.org/10.1126/science.1118923.

Attree, N., Gutiérrez, P., Schuckart, C., Markkanen, J., Skorov, Y., Xin, Y., Bischoff, D., Gundlach, B., Blum, J., 2025. Constraints on the ejecting-crust activity model on comet 67P/Churyumov–Gerasimenko. Mon. Not. R. Astron. Soc. 541, 771–783. http://dx.doi.org/10.1093/mnras/staf1040, publisher: Oxford University Press (OUP).

Attree, N., Jorda, L., Groussin, O., Agarwal, J., Lasagni Manghi, R., Tortora, P., Zannoni, M., Marschall, R., 2023. Activity distribution of comet 67P/Churyumov-Gerasimenko from combined measurements of non-gravitational forces and torques. Astron. Astrophys. 670, A170. http://dx.doi.org/10.1051/0004-6361/202245243.

Attree, N., Schuckart, C., Bischoff, D., Gundlach, B., Blum, J., 2024. Localized ejection of dust and chunks on comet 67P/Churyumov–Gerasimenko: testing how comets work. Mon. Not. R. Astron. Soc. 535, 65–77. http://dx.doi.org/10.1093/mnras/stae2315.

Auger, A.T., Groussin, O., Jorda, L., Bouley, S., Gaskell, R., Lamy, P.L., Capanna, C., Thomas, N., Pommerol, A., Sierks, H., Barbieri, C., Rodrigo, R., Koschny, D., Rickman, H., Keller, H.U., Agarwal, J., A'Hearn, M.F., Barucci, M.A., Bertaux, J.L., Bertini, I., Cremonese, G., Da Deppo, V., Davidsson, B., Debei, S., De Cecco, M., El-Maarry, M.R., Fornasier, S., Fulle, M., Gutiérrez, P.J., Güttler, C., Hviid, S., Ip, W.H., Knollenberg, J., Kramm, J.R., Kührt, E., Küppers, M., La Forgia, F., Lara, L.M., Lazzarin, M., Lopez Moreno, J.J., Marchi, S., Marzari, F., Massironi, M., Michalik, H., Naletto, G., Oklay, N., Pajola, M., Sabau, L., Tubiana, C., Vincent, J.B., Wenzel, K.P., 2015. Geomorphology of the Imhotep region on comet 67P/Churyumov-Gerasimenko from OSIRIS observations. Astron. Astrophys. 583, A35. http://dx.doi.org/10.1051/0004-6361/201525947.

Ayachit, U., 2015. The ParaView Guide: A Parallel Visualization Application. Kitware, Inc., Clifton Park, NY, USA.

Barrington, M.N., Birch, S.P.D., Jindal, A., Hayes, A.G., Corlies, P., Vincent, J.B., 2023. Quantifying morphological changes and sediment transport pathways on comet 67P/Churyumov-Gerasimenko. J. Geophys. Res.: Planets 128, e2022JE007723. http://dx.doi.org/10.1029/2022JE007723.

Belton, M.J., Melosh, J., 2009. Fluidization and multiphase transport of particulate cometary material as an explanation of the smooth terrains and repetitive outbursts on 9P/Tempel 1. Icarus 200, 280–291. http://dx.doi.org/10.1016/j.icarus.2008.11.012.

Bibring, J.P., Langevin, Y., Carter, J., Eng, P., Gondet, B., Jorda, L., Le Mouélic, S., Mottola, S., Pilorget, C., Poulet, F., Vincendon, M., 2015. 67P/Churyumov-Gerasimenko surface properties as derived from CIVA panoramic images. Science 349, aab0671. http://dx.doi.org/10.1126/science.aab0671.

Birch, S.P.D., Hayes, A.G., Umurhan, O.M., Tang, Y., Vincent, J., Oklay, N., Bodewits, D., Davidsson, B., Marschall, R., Soderblom, J.M., Moore, J.M., Corlies, P.M., Squyres, S.W., 2019. Migrating scarps as a significant driver for cometary surface evolution. Geophys. Res. Lett. 46, 12794–12804. http://dx.doi.org/10.1029/2019GL083982.

Birch, S.P.D., Tang, Y., Hayes, A.G., Kirk, R.L., Bodewits, D., Campins, H., Fernandez, Y., De Freitas Bart, R., Kutsop, N.W., Sierks, H., Soderblom, J.M., Squyres, S.W., Vincent, J.B., 2017. Geomorphology of comet 67P/Churyumov–Gerasimenko. Mon. Not. R. Astron. Soc. 469, S50–S67. http://dx.doi.org/10.1093/mnras/stx1096.

Bischoff, D., Schuckart, C., Attree, N., Gundlach, B., Blum, J., 2023. A quantitative description of comet 67P's dust and gas production remains enigmatic. Mon. Not. R. Astron. Soc. 523, 5171–5186. http://dx.doi.org/10.1093/mnras/stad1766.

Bouquety, A., Jorda, L., Groussin, O., Sejourné, A., Bouley, S., Costard, F., 2021. Ancient and present surface evolution processes in the Ash region of comet 67P/Churyumov-Gerasimenko. Astron. Astrophys. 649, A82. http://dx.doi.org/10.1051/0004-6361/202140516.

Braga, L., Amarante, A., Ferreira, A., Gomes, C., Ceranto, L., 2025. Equilibrium points and surface dynamics about comet 67P/Churyumov–Gerasimenko. Eur. Phys. J. Spec. Top. http://dx.doi.org/10.1140/epjs/s11734-025-01986-1.

Cambianica, P., Fulle, M., Cremonese, G., Simioni, E., Naletto, G., Massironi, M., Penasa, L., Lucchetti, A., Pajola, M., Bertini, I., Bodewits, D., Ceccarelli, C., Ferri, F., Fornasier, S., Frattin, E., Güttler, C., Gutiérrez, P.J., Keller, H.U., Kührt, E., Küppers, M., La Forgia, F., Lazzarin, M., Marzari, F., Mottola, S., Sierks, H., Toth, I., Tubiana, C., Vincent, J.B., 2020. Time evolution of dust deposits in the Hapi region of comet 67P/Churyumov-Gerasimenko. Astron. Astrophys. 636, A91. http://dx.doi.org/10.1051/0004-6361/202037485.

Choukroun, M., Altwegg, K., Kührt, E., Biver, N., Bockelée-Morvan, D., Drążkowska, J., Hérique, A., Hilchenbach, M., Marschall, R., Pätzold, M., Taylor, M.G.G.T., Thomas, N., 2020. Dust-to-gas and refractory-to-ice mass ratios of comet 67P/Churyumov-Gerasimenko from Rosetta observations. Space Sci. Rev. 216, 44. http://dx.doi.org/10.1007/s11214-020-00662-1.

Davidsson, B.J., Birch, S., Blake, G.A., Bodewits, D., Dworkin, J.P., Glavin, D.P., Furukawa, Y., Lunine, J.I., Mitchell, J.L., Nguyen, A.N., Squyres, S., Takigawa, A., Vincent, J.B., Zacny, K., 2021. Airfall on comet 67P/Churyumov–Gerasimenko. Icarus 354, 114004. http://dx.doi.org/10.1016/j.icarus.2020.114004.

Davidsson, B.J.R., Schloerb, F.P., Fornasier, S., Oklay, N., Gutiérrez, P.J., Buratti, B.J., Chmielewski, A.B., Gulkis, S., Hofstadter, M.D., Keller, H.U., Sierks, H., Güttler, C., Küppers, M., Rickman, H., Choukroun, M., Lee, S., Lellouch, E., Lethuillier, A., Da Deppo, V., Groussin, O., Kührt, E., Thomas, N., Tubiana, C., El-Maarry, M.R., La Forgia, F., Mottola, S., Pajola, M., 2022. CO2-driven surface changes in the Hapi region on Comet 67P/Churyumov–Gerasimenko. Mon. Not. R. Astron. Soc. 516, 6009–6040. http://dx.doi.org/10.1093/mnras/stac2560.

Dietrich, W.E., Bellugi, D.G., Sklar, L.S., Stock, J.D., Heimsath, A.M., Roering, J.J., 2013. Geomorphic transport laws for predicting landscape form and dynamics. In: Wilcock, P.R., Iverson, R.M. (Eds.), Geophysical Monograph Series. American Geophysical Union, Washington, D. C, pp. 103–132. http://dx.doi.org/10.1029/135GM09.

El-Maarry, M.R., Groussin, O., Keller, H.U., Thomas, N., Vincent, J.B., Mottola, S., Pajola, M., Otto, K., Herny, C., Krasilnikov, S., 2019. Surface morphology of comets and associated evolutionary processes: A review of Rosetta's observations of 67P/Churyumov–Gerasimenko. Space Sci. Rev. 215, 36. http://dx.doi.org/10.1007/s11214-019-0602-1.

El-Maarry, M.R., Groussin, O., Thomas, N., Pajola, M., Auger, A.T., Davidsson, B., Hu, X., Hviid, S.F., Knollenberg, J., Güttler, C., Tubiana, C., Fornasier, S., Feller, C., Hasselmann, P., Vincent, J.B., Sierks, H., Barbieri, C., Lamy, P., Rodrigo, R., Koschny, D., Keller, H.U., Rickman, H., A'Hearn, M.F., Barucci, M.A., Bertaux, J.L., Bertini, I., Besse, S., Bodewits, D., Cremonese, G., Da Deppo, V., Debei, S., De Cecco, M., Deller, J., Deshapriya, J.D.P., Fulle, M., Gutierrez, P.J., Hofmann, M., Ip, W.H., Jorda, L., Kovacs, G., Kramm, J.R., Kührt, E., Küppers, M., Lara, L.M., Lazzarin, M., Lin, Z.Y., Lopez Moreno, J.J., Marchi, S., Marzari, F., Mottola, S., Naletto, G., Oklay, N., Pommerol, A., Preusker, F., Scholten, F., Shi, X., 2017. Surface changes on comet 67P/Churyumov-Gerasimenko suggest a more active past. Science 355, 1392–1395. http://dx.doi.org/10.1126/science.aak9384.

El-Maarry, M.R., Thomas, N., Giacomini, L., Massironi, M., Pajola, M., Marschall, R., Gracia-Berná, A., Sierks, H., Barbieri, C., Lamy, P.L., Rodrigo, R., Rickman, H.,

Koschny, D., Keller, H.U., Agarwal, J., A'Hearn, M.F., Auger, A.T., Barucci, M.A., Bertaux, J.L., Bertini, I., Besse, S., Bodewits, D., Cremonese, G., Da Deppo, V., Davidsson, B., De Cecco, M., Debei, S., Güttler, C., Fornasier, S., Fulle, M., Groussin, O., Gutierrez, P.J., Hviid, S.F., Ip, W.H., Jorda, L., Knollenberg, J., Kovacs, G., Kramm, J.R., Kührt, E., Küppers, M., La Forgia, F., Lara, L.M., Lazzarin, M., Lopez Moreno, J.J., Marchi, S., Marzari, F., Michalik, H., Naletto, G., Oklay, N., Pommerol, A., Preusker, F., Scholten, F., Tubiana, C., Vincent, J.B., 2015. Regional surface morphology of comet 67P/Churyumov-Gerasimenko from Rosetta/OSIRIS images. Astron. Astrophys. 583, A26. http://dx.doi.org/10.1051/0004-6361/201525723.

El-Maarry, M.R., Thomas, N., Gracia-Berná, A., Pajola, M., Lee, J.C., Massironi, M., Davidsson, B., Marchi, S., Keller, H.U., Hviid, S.F., Besse, S., Sierks, H., Barbieri, C., Lamy, P.L., Koschny, D., Rickman, H., Rodrigo, R., A'Hearn, M.F., Auger, A.T., Barucci, M.A., Bertaux, J.L., Bertini, I., Bodewits, D., Cremonese, G., Da Deppo, V., De Cecco, M., Debei, S., Güttler, C., Fornasier, S., Fulle, M., Giacomini, L., Groussin, O., Gutierrez, P.J., Ip, W.H., Jorda, L., Knollenberg, J., Kovacs, G., Kramm, J.R., Kührt, E., Küppers, M., Lara, L.M., Lazzarin, M., Lopez Moreno, J.J., Marschall, R., Marzari, F., Naletto, G., Oklay, N., Pommerol, A., Preusker, F., Scholten, F., Tubiana, C., Vincent, J.B., 2016. Regional surface morphology of comet 67P/Churyumov-Gerasimenko from Rosetta/OSIRIS images: The southern hemisphere. Astron. Astrophys. 593, A110. http://dx.doi.org/10.1051/0004-6361/201628634.

Fougere, N., Altwegg, K., Berthelier, J.J., Bieler, A., Bockelée-Morvan, D., Calmonte, U., Capaccioni, F., Combi, M.R., De Keyser, J., Debout, V., Erard, S., Fiethe, B., Filacchione, G., Fink, U., Fuselier, S.A., Gombosi, T.I., Hansen, K.C., Hässig, M., Huang, Z., Le Roy, L., Leyrat, C., Migliorini, A., Piccioni, G., Rinaldi, G., Rubin, M., Shou, Y., Tenishev, V., Toth, G., Tzou, C.Y., the VIRTIS team, the ROSINA team, 2016. Three-dimensional direct simulation Monte-Carlo modeling of the coma of comet 67P/Churyumov-Gerasimenko observed by the VIRTIS and ROSINA instruments on board Rosetta. Astron. Astrophys. 588, A134. http://dx.doi.org/10.1051/0004-6361/201527889.

Fulle, M., Blum, J., Rotundi, A., 2019. How comets work. Astrophys. J. Lett. 879, L8. http://dx.doi.org/10.3847/2041-8213/ab2898.

Groussin, O., Jorda, L., Attree, N., Birch, S.P.D., Bürger, J., Gutiérrez, P., Jindal, A.S., Keller, H.U., Kramer, T., Manghi, R.L., Läuter, M., Markkanen, J., Marschall, R., Schuckart, C., 2025. Thermal environment and erosion of comet 67P/Churyumov-Gerasimenko. Astron. Astrophys. 694, A21. http://dx.doi.org/10.1051/0004-6361/202452260.

Groussin, O., Sierks, H., Barbieri, C., Lamy, P., Rodrigo, R., Koschny, D., Rickman, H., Keller, H.U., A'Hearn, M.F., Auger, A.T., Barucci, M.A., Bertaux, J.L., Bertini, I., Besse, S., Cremonese, G., Da Deppo, V., Davidsson, B., Debei, S., De Cecco, M., El-Maarry, M.R., Fornasier, S., Fulle, M., Gutiérrez, P.J., Güttler, C., Hviid, S., Ip, W.H., Jorda, L., Knollenberg, J., Kovacs, G., Kramm, J.R., Kührt, E., Küppers, M., Lara, L.M., Lazzarin, M., Lopez Moreno, J.J., Lowry, S., Marchi, S., Marzari, F., Massironi, M., Mottola, S., Naletto, G., Oklay, N., Pajola, M., Pommerol, A., Thomas, N., Toth, I., Tubiana, C., Vincent, J.B., 2015. Temporal morphological changes in the Imhotep region of comet 67P/Churyumov-Gerasimenko. Astron. Astrophys. 583, A36. http://dx.doi.org/10.1051/0004-6361/201527020.

Gundlach, B., Fulle, M., Blum, J., 2020. On the activity of comets: understanding the gas and dust emission from comet 67/Churyumov–Gerasimenko's south-pole region during perihelion. Mon. Not. R. Astron. Soc. 493, 3690–3715. http://dx.doi.org/10.1093/mnras/staa449.

Hermalyn, B., Farnham, T.L., Collins, S.M., Kelley, M.S., A'Hearn, M.F., Bodewits, D., Carcich, B., Lindler, D.J., Lisse, C., Meech, K., Schultz, P.H., Thomas, P.C., 2013. The detection, localization, and dynamics of large icy particles surrounding Comet 103P/Hartley 2. Icarus 222, 625–633. http://dx.doi.org/10.1016/j.icarus.2012.09.030.

Hu, X., Shi, X., Sierks, H., Fulle, M., Blum, J., Keller, H.U., Kührt, E., Davidsson, B., Güttler, C., Gundlach, B., Pajola, M., Bodewits, D., Vincent, J.B., Oklay, N., Massironi, M., Fornasier, S., Tubiana, C., Groussin, O., Boudreault, S., Höfner, S., Mottola, S., Barbieri, C., Lamy, P.L., Rodrigo, R., Koschny, D., Rickman, H., A'Hearn, M., Agarwal, J., Barucci, M.A., Bertaux, J.L., Bertini, I., Cremonese, G., Da Deppo, V., Debei, S., De Cecco, M., Deller, J., El-Maarry, M.R., Gicquel, A., Gutierrez-Marques, P., Gutiérrez, P.J., Hofmann, M., Hviid, S.F., Ip, W.H., Jorda, L., Knollenberg, J., Kovacs, G., Kramm, J.R., Küppers, M., Lara, L.M., Lazzarin, M., Lopez-Moreno, J.J., Marzari, F., Naletto, G., Thomas, N., 2017. Seasonal erosion and restoration of the dust cover on comet 67P/Churyumov-Gerasimenko as observed by OSIRIS onboard Rosetta. Astron. Astrophys. 604, A114. http://dx.doi.org/10.1051/0004-6361/201629910.

Jewitt, D., Agarwal, J., Hui, M.T., Li, J., Mutchler, M., Weaver, H., 2019. Distant comet C/2017 K2 and the cohesion bottleneck. Astron. J. 157, 65. http://dx.doi.org/10.3847/1538-3881/aaf38c.

Jindal, A., 2025a. abhinav-s-jindal/67p_sediment_transport_pathways: Initial release - comet 67p sediment transport analysis. http://dx.doi.org/10.5281/zenodo.17574889.

Jindal, A., 2025b. Comet 67p sediment transport dictionaries. http://dx.doi.org/10.5281/zenodo.17574912.

Jindal, A.S., Birch, S.P.D., Hayes, A.G., Özyurt, F.P., Issah, A.B., Moruzzi, S.A., Barrington, M.N., Soderblom, J.M., Kirk, R.L., Marschall, R., Vincent, J.B., 2024. Measuring erosional and depositional patterns across comet 67P's Imhotep region. J. Geophys. Res.: Planets 129, e2023JE008089. http://dx.doi.org/10.1029/2023JE008089.

Jindal, A.S., Birch, S.P.D., Hayes, A.G., Umurhan, O.M., Marschall, R., Soderblom, J.M., Vincent, J.B., Bodewits, D., 2022. Topographically influenced evolution of large-scale changes in comet 67P/Churyumov–Gerasimenko's Imhotep region. Planet. Sci. J. 3, 193. http://dx.doi.org/10.3847/PSJ/ac7e48.

Jorda, L., Gaskell, R., Capanna, C., Hviid, S., Lamy, P., Ďurech, J., Faury, G., Groussin, O., Gutiérrez, P., Jackman, C., Keihm, S., Keller, H., Knollenberg, J., Kührt, E., Marchi, S., Mottola, S., Palmer, E., Schloerb, F., Sierks, H., Vincent, J.B., A'Hearn, M., Barbieri, C., Rodrigo, R., Koschny, D., Rickman, H., Barucci, M., Bertaux, J., Bertini, I., Cremonese, G., Da Deppo, V., Davidsson, B., Debei, S., De Cecco, M., Fornasier, S., Fulle, M., Güttler, C., Ip, W.H., Kramm, J., Küppers, M., Lara, L., Lazzarin, M., Lopez Moreno, J., Marzari, F., Naletto, G., Oklay, N., Thomas, N., Tubiana, C., Wenzel, K.P., 2016. The global shape, density and rotation of Comet 67P/Churyumov-Gerasimenko from preperihelion Rosetta/OSIRIS observations. Icarus 277, 257–278. http://dx.doi.org/10.1016/j.icarus.2016.05.002.

Keller, H.U., Kührt, E., 2020. Cometary nuclei—From Giotto to Rosetta. Space Sci. Rev. 216, 14. http://dx.doi.org/10.1007/s11214-020-0634-6.

Keller, H.U., Mottola, S., Davidsson, B., Schröder, S.E., Skorov, Y., Kührt, E., Groussin, O., Pajola, M., Hviid, S.F., Preusker, F., Scholten, F., A'Hearn, M.F., Sierks, H., Barbieri, C., Lamy, P., Rodrigo, R., Koschny, D., Rickman, H., Barucci, M.A., Bertaux, J.L., Bertini, I., Cremonese, G., Da Deppo, V., Debei, S., De Cecco, M., Fornasier, S., Fulle, M., Gutiérrez, P.J., Ip, W.H., Jorda, L., Knollenberg, J., Kramm, J.R., Küppers, M., Lara, L.M., Lazzarin, M., Lopez Moreno, J.J., Marzari, F., Michalik, H., Naletto, G., Sabau, L., Thomas, N., Vincent, J.B., Wenzel, K.P., Agarwal, J., Güttler, C., Oklay, N., Tubiana, C., 2015. Insolation, erosion, and morphology of comet 67P/Churyumov-Gerasimenko. Astron. Astrophys. 583, A34. http://dx.doi.org/10.1051/0004-6361/201525964.

Keller, H.U., Mottola, S., Hviid, S.F., Agarwal, J., Kührt, E., Skorov, Y., Otto, K., Vincent, J.B., Oklay, N., Schröder, S.E., Davidsson, B., Pajola, M., Shi, X., Bodewits, D., Toth, I., Preusker, F., Scholten, F., Sierks, H., Barbieri, C., Lamy, P., Rodrigo, R., Koschny, D., Rickman, H., A'Hearn, M.F., Barucci, M.A., Bertaux, J.L., Bertini, I., Cremonese, G., Da Deppo, V., Debei, S., De Cecco, M., Deller, J., Fornasier, S., Fulle, M., Groussin, O., Gutiérrez, P.J., Güttler, C., Hofmann, M., Ip, W.H., Jorda, L., Knollenberg, J., Kramm, J.R., Küppers, M., Lara, L.M., Lazzarin, M., Lopez-Moreno, J.J., Marzari, F., Naletto, G., Tubiana, C., Thomas, N., 2017. Seasonal mass transfer on the nucleus of comet 67P/Chuyumov–Gerasimenko. Mon. Not. R. Astron. Soc. 469, S357–S371. http://dx.doi.org/10.1093/mnras/stx1726.

Kloos, J.L., Farnham, T.L., Sunshine, J.M., Rizos, J.L., 2025. Investigating local- and global-scale dust redistribution on comet 67P/Churyumov–Gerasimenko. Planet. Sci. J. 6, 268. http://dx.doi.org/10.3847/PSJ/ae1739.

Kramer, T., Läuter, M., Hviid, S., Jorda, L., Keller, H.U., Kührt, E., 2019. Comet 67P/Churyumov-Gerasimenko rotation changes derived from sublimation-induced torques. Astron. Astrophys. 630, A3. http://dx.doi.org/10.1051/0004-6361/201834349.

Kührt, E., Keller, H., 1994. The formation of cometary surface crusts. Icarus 109, 121–132. http://dx.doi.org/10.1006/icar.1994.1080.

Lai, I.L., Ip, W.H., Su, C.C., Wu, J.S., Lee, J.C., Lin, Z.Y., Liao, Y., Thomas, N., Sierks, H., Barbieri, C., Lamy, P., Rodrigo, R., Koschny, D., Rickman, H., Keller, H.U., Agarwal, J., A'Hearn, M.F., Barucci, M.A., Bertaux, J.L., Bertini, I., Boudreault, S., Cremonese, G., Da Deppo, V., Davidsson, B., Debei, S., De Cecco, M., Deller, J., Fornasier, S., Fulle, M., Groussin, O., Gutiérrez, P.J., Güttler, C., Hofmann, M., Hviid, S.F., Jorda, L., Knollenberg, J., Kovacs, G., Kramm, J.R., Kührt, E., Küppers, M., Lara, L.M., Lazzarin, M., Lopez Moreno, J.J., Marzari, F., Naletto, G., Oklay, N., Shi, X., Tubiana, C., Vincent, J.B., 2016. Gas outflow and dust transport of comet 67P/Churyumov–Gerasimenko. Mon. Not. R. Astron. Soc. 462, S533–S546. http://dx.doi.org/10.1093/mnras/stx332.

Lara, L.M., Lowry, S., Vincent, J.B., Gutiérrez, P.J., Rożek, A., La Forgia, F., Oklay, N., Sierks, H., Barbieri, C., Lamy, P.L., Rodrigo, R., Koschny, D., Rickman, H., Keller, H.U., Agarwal, J., Auger, A.T., A'Hearn, M.F., Barucci, M.A., Bertaux, J.L., Bertini, I., Besse, S., Bodewits, D., Cremonese, G., Davidsson, B., Da Deppo, V., Debei, S., De Cecco, M., El-Maarry, M.R., Ferri, F., Fornasier, S., Fulle, M., Groussin, O., Gutiérrez-Marques, P., Güttler, C., Hviid, S.F., Ip, W.H., Jorda, L., Knollenberg, J., Kovacs, G., Kramm, J.R., Kührt, E., Küppers, M., Lazzarin, M., Lin, Z.Y., López-Moreno, J.J., Magrin, S., Marzari, F., Michalik, H., Moissl-Fraund, R., Moreno, F., Mottola, S., Naletto, G., Pajola, M., Pommerol, A., Thomas, N., Sabau, M.D., Tubiana, C., 2015. Large-scale dust jets in the coma of 67P/Churyumov-Gerasimenko as seen by the OSIRIS instrument onboard Rosetta. Astron. Astrophys. 583, A9. http://dx.doi.org/10.1051/0004-6361/201526103.

Marschall, R., Markkanen, J., Gerig, S.B., Pinzón-Rodríguez, O., Thomas, N., Wu, J.S., 2020. The dust-to-gas ratio, size distribution, and dust fall-back fraction of comet 67P/Churyumov-Gerasimenko: Inferences from linking the optical and dynamical properties of the inner comae. Front. Phys. 8, 227. http://dx.doi.org/10.3389/fphy.2020.00227.

Marschall, R., Su, C.C., Liao, Y., Thomas, N., Altwegg, K., Sierks, H., Ip, W.H., Keller, H.U., Knollenberg, J., Kührt, E., Lai, I.L., Rubin, M., Skorov, Y., Wu, J.S., Jorda, L., Preusker, F., Scholten, F., Gracia-Berná, A., Gicquel, A., Naletto, G., Shi, X., Vincent, J.B., 2016. Modelling observations of the inner gas and dust coma of comet 67P/Churyumov-Gerasimenko using ROSINA/COPS and OSIRIS data: First results. Astron. Astrophys. 589, A90. http://dx.doi.org/10.1051/0004-6361/201628085.

Möhlmann, D., 1994. Surface regolith and environment of comets. Planet. Space Sci. 42, 933–937. http://dx.doi.org/10.1016/0032-0633(94)90053-1.

Molaro, J.L., Hergenrother, C.W., Chesley, S.R., Walsh, K.J., Hanna, R.D., Haberle, C.W., Schwartz, S.R., Ballouz, R., Bottke, W.F., Campins, H.J., Lauretta, D.S., 2020. Thermal fatigue as a driving mechanism for activity on asteroid Bennu. J. Geophys. Res.: Planets 125, e2019JE006325. http://dx.doi.org/10.1029/2019JE006325.

Mottola, S., Arnold, G., Grothues, H.G., Jaumann, R., Michaelis, H., Neukum, G., Bibring, J.P., Schröder, S.E., Hamm, M., Otto, K.A., Pelivan, I., Proffe, G., Scholten, F., Tirsch, D., Kreslavsky, M., Remetean, E., Souvannavong, F., Dolives, B., 2015. The structure of the regolith on 67P/Churyumov-Gerasimenko from ROLIS descent imaging. Science 349, aab0232. http://dx.doi.org/10.1126/science.aab0232.

Pajola, M., Höfner, S., Vincent, J.B., Oklay, N., Scholten, F., Preusker, F., Mottola, S., Naletto, G., Fornasier, S., Lowry, S., Feller, C., Hasselmann, P.H., Güttler, C., Tubiana, C., Sierks, H., Barbieri, C., Lamy, P., Rodrigo, R., Koschny, D., Rickman, H., Keller, H.U., Agarwal, J., A'Hearn, M.F., Barucci, M.A., Bertaux, J.L., Bertini, I., Besse, S., Boudreault, S., Cremonese, G., Da Deppo, V., Davidsson, B., Debei, S., De Cecco, M., Deller, J., Deshapriya, J.D.P., El-Maarry, M.R., Ferrari, S., Ferri, F., Fulle, M., Groussin, O., Gutierrez, P., Hofmann, M., Hviid, S.F., Ip, W.H., Jorda, L., Knollenberg, J., Kovacs, G., Kramm, J.R., Kührt, E., Küppers, M., Lara, L.M., Lin, Z.Y., Lazzarin, M., Lucchetti, A., Lopez Moreno, J.J., Marzari, F., Massironi, M., Michalik, H., Penasa, L., Pommerol, A., Simioni, E., Thomas, N., Toth, I., Baratti, E., 2017a. The pristine interior of comet 67P revealed by the combined Aswan outburst and cliff collapse. Nat. Astron. 1, 0092. http://dx.doi.org/10.1038/s41550-017-0092.

Pajola, M., Lucchetti, A., Fulle, M., Mottola, S., Hamm, M., Da Deppo, V., Penasa, L., Kovacs, G., Massironi, M., Shi, X., Tubiana, C., Güttler, C., Oklay, N., Vincent, J.B., Toth, I., Davidsson, B., Naletto, G., Sierks, H., Barbieri, C., Lamy, P.L., Rodrigo, R., Koschny, D., Rickman, H., Keller, H.U., Agarwal, J., A'Hearn, M.F., Barucci, M.A., Bertaux, J.L., Bertini, I., Cremonese, G., Debei, S., De Cecco, M., Deller, J., El Maarry, M.R., Fornasier, S., Frattin, E., Gicquel, A., Groussin, O., Gutierrez, P.J., Höfner, S., Hofmann, M., Hviid, S.F., Ip, W.H., Jorda, L., Knollenberg, J., Kramm, J.R., Kührt, E., Küppers, M., Lara, L.M., Lazzarin, M., Moreno, J.J.L., Marzari, F., Michalik, H., Preusker, F., Scholten, F., Thomas, N., 2017b. The pebbles/boulders size distributions on Sais: Rosetta's final landing site on comet 67P/Churyumov–Gerasimenko. Mon. Not. R. Astron. Soc. 469, S636–S645. http://dx.doi.org/10.1093/mnras/stx1620.

Pajola, M., Mottola, S., Hamm, M., Fulle, M., Davidsson, B., Güttler, C., Sierks, H., Naletto, G., Arnold, G., Grothues, H.G., Jaumann, R., Michaelis, H., Bibring, J.P., Barbieri, C., Lamy, P.L., Rodrigo, R., Koschny, D., Rickman, H., Keller, H.U., Agarwal, J., A'Hearn, M.F., Barucci, M.A., Bertaux, J.L., Bertini, I., Boudreault, S., Cremonese, G., Da Deppo, V., Debei, S., De Cecco, M., Deller, J., El Maarry, M.R., Feller, C., Fornasier, S., Gicquel, A., Groussin, O., Gutierrez, P.J., Hofmann, M., Hviid, S.F., Ip, W.H., Jorda, L., Knollenberg, J., Kramm, J.R., Kührt, E., Küppers, M., La Forgia, F., Lara, L.M., Lin, Z.Y., Lazzarin, M., Lopez Moreno, J.J., Lucchetti, A., Marzari, F., Massironi, M., Michalik, H., Oklay, N., Pommerol, A., Preusker, F., Scholten, F., Thomas, N., Tubiana, C., Vincent, J.B., 2016. The Agilkia boulders/pebbles size–frequency distributions: OSIRIS and ROLIS joint observations of 67P surface. Mon. Not. R. Astron. Soc. 462, S242–S252. http://dx.doi.org/10.1093/mnras/stw2720.

Pajola, M., Vincent, J.B., Güttler, C., Lee, J.C., Bertini, I., Massironi, M., Simioni, E., Marzari, F., Giacomini, L., Lucchetti, A., Barbieri, C., Cremonese, G., Naletto, G., Pommerol, A., El-Maarry, M.R., Besse, S., Küppers, M., La Forgia, F., Lazzarin, M., Thomas, N., Auger, A.T., Sierks, H., Lamy, P., Rodrigo, R., Koschny, D., Rickman, H., Keller, H.U., Agarwal, J., A'Hearn, M.F., Barucci, M.A., Bertaux, J.L., Deppo, V.D., Davidsson, B., De Cecco, M., Debei, S., Ferri, F., Fornasier, S., Fulle, M., Groussin, O., Gutierrez, P.J., Hviid, S.F., Ip, W.H., Jorda, L., Knollenberg, J., Kramm, J.R., Kürt, E., Lara, L.M., Lin, Z.Y., Moreno, J.J.L., Magrin, S., Marchi, S., Michalik, H., Moissl, R., Mottola, S., Oklay, N., Preusker, F., Scholten, F., Tubiana, C., 2015. Size-frequency distribution of boulders ≥7 m on comet 67P/Churyumov-Gerasimenko. Astron. Astrophys. 583, A37. http://dx.doi.org/10.1051/0004-6361/201525975.

Pätzold, M., Andert, T.P., Hahn, M., Barriot, J.P., Asmar, S.W., Häusler, B., Bird, M.K., Tellmann, S., Oschlisniok, J., Peter, K., 2019. The Nucleus of comet 67P/Churyumov–Gerasimenko – Part I: The global view – nucleus mass, mass-loss, porosity, and implications. Mon. Not. R. Astron. Soc. 483, 2337–2346. http://dx.doi.org/10.1093/mnras/sty3171.

Perron, J.T., Kirchner, J.W., Dietrich, W.E., 2008. Spectral signatures of characteristic spatial scales and nonfractal structure in landscapes. J. Geophys. Res.: Earth Surf. 113, 2007JF000866. http://dx.doi.org/10.1029/2007JF000866.

Preusker, F., Scholten, F., Matz, K.D., Roatsch, T., Hviid, S.F., Mottola, S., Knollenberg, J., Kührt, E., Pajola, M., Oklay, N., Vincent, J.B., Davidsson, B., A'Hearn, M.F., Agarwal, J., Barbieri, C., Barucci, M.A., Bertaux, J.L., Bertini, I., Cremonese, G., Da Deppo, V., Debei, S., De Cecco, M., Fornasier, S., Fulle, M., Groussin, O., Gutiérrez, P.J., Güttler, C., Ip, W.H., Jorda, L., Keller, H.U., Koschny, D., Kramm, J.R., Küppers, M., Lamy, P., Lara, L.M., Lazzarin, M., Lopez Moreno, J.J., Marzari, F., Massironi, M., Naletto, G., Rickman, H., Rodrigo, R., Sierks, H., Thomas, N., Tubiana, C., 2017. The global meter-level shape model of comet 67P/Churyumov-Gerasimenko. Astron. Astrophys. 607, L1. http://dx.doi.org/10.1051/0004-6361/201731798.

Rotundi, A., Sierks, H., Della Corte, V., Fulle, M., Gutierrez, P.J., Lara, L., Barbieri, C., Lamy, P.L., Rodrigo, R., Koschny, D., Rickman, H., Keller, H.U., López-Moreno, J.J., Accolla, M., Agarwal, J., A'Hearn, M.F., Altobelli, N., Angrilli, F., Barucci, M.A., Bertaux, J.L., Bertini, I., Bodewits, D., Bussoletti, E., Colangeli, L., Cosi, M., Cremonese, G., Crifo, J.F., Da Deppo, V., Davidsson, B., Debei, S., De Cecco, M., Esposito, F., Ferrari, M., Fornasier, S., Giovane, F., Gustafson, B., Green, S.F., Groussin, O., Grün, E., Güttler, C., Herranz, M.L., Hviid, S.F., Ip, W., Ivanovski, S., Jerónimo, J.M., Jorda, L., Knollenberg, J., Kramm, R., Kührt, E., Küppers, M., Lazzarin, M., Leese, M.R., López-Jiménez, A.C., Lucarelli, F., Lowry, S.C., Marzari, F., Epifani, E.M., McDonnell, J.A.M., Mennella, V., Michalik, H., Molina, A., Morales, R., Moreno, F., Mottola, S., Naletto, G., Oklay, N., Ortiz, J.L., Palomba, E., Palumbo, P., Perrin, J.M., Rodríguez, J., Sabau, L., Snodgrass, C., Sordini, R., Thomas, N., Tubiana, C., Vincent, J.B., Weissman, P., Wenzel, K.P., Zakharov, V., Zarnecki, J.C., 2015. Dust measurements in the coma of comet 67P/Churyumov-Gerasimenko inbound to the Sun. Science 347, aaa3905. http://dx.doi.org/10.1126/science.aaa3905.

Schuckart, C., Blum, J., 2025. The release of micron-sized dust grains from evaporating micro-granular dust-ice mixtures: Applications to cometary activity and protoplanetary disks. Astron. Astrophys. 697, A205. http://dx.doi.org/10.1051/0004-6361/202553750.

Sierks, H., Barbieri, C., Lamy, P.L., Rodrigo, R., Koschny, D., Rickman, H., Keller, H.U., Agarwal, J., A'Hearn, M.F., Angrilli, F., Auger, A.T., Barucci, M.A., Bertaux, J.L., Bertini, I., Besse, S., Bodewits, D., Capanna, C., Cremonese, G., Da Deppo, V., Davidsson, B., Debei, S., De Cecco, M., Ferri, F., Fornasier, S., Fulle, M., Gaskell, R., Giacomini, L., Groussin, O., Gutierrez-Marques, P., Gutiérrez, P.J., Güttler, C., Hoekzema, N., Hviid, S.F., Ip, W.H., Jorda, L., Knollenberg, J., Kovacs, G., Kramm, J.R., Kührt, E., Küppers, M., La Forgia, F., Lara, L.M., Lazzarin, M., Leyrat, C., Lopez Moreno, J.J., Magrin, S., Marchi, S., Marzari, F., Massironi, M., Michalik, H., Moissl, R., Mottola, S., Naletto, G., Oklay, N., Pajola, M., Pertile, M., Preusker, F., Sabau, L., Scholten, F., Snodgrass, C., Thomas, N., Tubiana, C., Vincent, J.B., Wenzel, K.P., Zaccariotto, M., Pätzold, M., 2015. On the nucleus structure and activity of comet 67P/Churyumov-Gerasimenko. Science 347, aaa1044. http://dx.doi.org/10.1126/science.aaa1044.

Skorov, Y., Reshetnyk, V., Lacerda, P., Hartogh, P., Blum, J., 2016. Acceleration of cometary dust near the nucleus: application to 67P/Churyumov–Gerasimenko. Mon. Not. R. Astron. Soc. 461, 3410–3420. http://dx.doi.org/10.1093/mnras/stw1470.

Soderblom, L.A., Becker, T.L., Bennett, G., Boice, D.C., Britt, D.T., Brown, R.H., Buratti, B.J., Isbell, C., Giese, B., Hare, T., Hicks, M.D., Howington-Kraus, E., Kirk, R.L., Lee, M., Nelson, R.M., Oberst, J., Owen, T.C., Rayman, M.D., Sandel, B.R., Stern, S.A., Thomas, N., Yelle, R.V., 2002. Observations of Comet 19P/Borrelly by the miniature integrated camera and spectrometer aboard deep space 1. Science 296, 1087–1091. http://dx.doi.org/10.1126/science.1069527.

Squyres, S.W., Nakamura-Messenger, K., Mitchell, D.F., Moran, V.E., Houghton, M.B., Glavin, D.P., Hayes, A.G., Lauretta, D.S., Caesar Project Team, 2018. The CAESAR new frontiers mission: 1. Overview. In: 49th Annual Lunar and Planetary Science Conference. p. 1332.

Steckloff, J.K., Johnson, B.C., Bowling, T., Jay Melosh, H., Minton, D., Lisse, C.M., Battams, K., 2015. Dynamic sublimation pressure and the catastrophic breakup of Comet ISON. Icarus 258, 430–437. http://dx.doi.org/10.1016/j.icarus.2015.06.032.

Thomas, P., A'Hearn, M.F., Veverka, J., Belton, M.J., Kissel, J., Klaasen, K.P., McFadden, L.A., Melosh, H.J., Schultz, P.H., Besse, S., Carcich, B.T., Farnham, T.L., Groussin, O., Hermalyn, B., Li, J.Y., Lindler, D.J., Lisse, C.M., Meech, K., Richardson, J.E., 2013. Shape, density, and geology of the nucleus of Comet 103P/Hartley 2. Icarus 222, 550–558. http://dx.doi.org/10.1016/j.icarus.2012.05.034.

Thomas, N., Davidsson, B., El-Maarry, M.R., Fornasier, S., Giacomini, L., Gracia-Berná, A.G., Hviid, S.F., Ip, W.H., Jorda, L., Keller, H.U., Knollenberg, J., Kührt, E., La Forgia, F., Lai, I.L., Liao, Y., Marschall, R., Massironi, M., Mottola, S., Pajola, M., Poch, O., Pommerol, A., Preusker, F., Scholten, F., Su, C.C., Wu, J.S., Vincent, J.B., Sierks, H., Barbieri, C., Lamy, P.L., Rodrigo, R., Koschny, D., Rickman, H., A'Hearn, M.F., Barucci, M.A., Bertaux, J.L., Bertini, I., Cremonese, G., Da Deppo, V., Debei, S., de Cecco, M., Fulle, M., Groussin, O., Gutierrez, P.J., Kramm, J.R., Küppers, M., Lara, L.M., Lazzarin, M., Lopez Moreno, J.J., Marzari, F., Michalik, H., Naletto, G., Agarwal, J., Güttler, C., Oklay, N., Tubiana, C., 2015a. Redistribution of particles across the nucleus of comet 67P/Churyumov-Gerasimenko. Astron. Astrophys. 583, A17. http://dx.doi.org/10.1051/0004-6361/201526049.

Thomas, N., El Maarry, M., Theologou, P., Preusker, F., Scholten, F., Jorda, L., Hviid, S., Marschall, R., Kührt, E., Naletto, G., Sierks, H., Lamy, P., Rodrigo, R., Koschny, D.,

Davidsson, B., Barucci, M., Bertaux, J., Bertini, I., Bodewits, D., Cremonese, G., Da Deppo, V., Debei, S., De Cecco, M., Fornasier, S., Fulle, M., Groussin, O., Gutièrrez, P., Güttler, C., Ip, W., Keller, H., Knollenberg, J., Lara, L., Lazzarin, M., Lòpez-Moreno, J., Marzari, F., Tubiana, C., Vincent, J., 2018. Regional unit definition for the nucleus of comet 67P/Churyumov-Gerasimenko on the SHAP7 model. Planet. Space Sci. 164, 19–36. http://dx.doi.org/10.1016/j.pss.2018.05.019.

Thomas, N., Sierks, H., Barbieri, C., Lamy, P.L., Rodrigo, R., Rickman, H., Koschny, D., Keller, H.U., Agarwal, J., A'Hearn, M.F., Angrilli, F., Auger, A.T., Barucci, M.A., Bertaux, J.L., Bertini, I., Besse, S., Bodewits, D., Cremonese, G., Da Deppo, V., Davidsson, B., De Cecco, M., Debei, S., El-Maarry, M.R., Ferri, F., Fornasier, S., Fulle, M., Giacomini, L., Groussin, O., Gutierrez, P.J., Güttler, C., Hviid, S.F., Ip, W.H., Jorda, L., Knollenberg, J., Kramm, J.R., Kührt, E., Küppers, M., La Forgia, F., Lara, L.M., Lazzarin, M., Moreno, J.J.L., Magrin, S., Marchi, S., Marzari, F., Massironi, M., Michalik, H., Moissl, R., Mottola, S., Naletto, G., Oklay, N., Pajola, M., Pommerol, A., Preusker, F., Sabau, L., Scholten, F., Snodgrass, C., Tubiana, C., Vincent, J.B., Wenzel, K.P., 2015b. The morphological diversity of comet 67P/Churyumov-Gerasimenko. Science 347, aaa0440. http://dx.doi.org/10.1126/science.aaa0440.

Thomas, P.C., Veverka, J., Belton, M.J., Hidy, A., A'Hearn, M.F., Farnham, T., Groussin, O., Li, J.Y., McFadden, L.A., Sunshine, J., Wellnitz, D., Lisse, C., Schultz, P., Meech, K.J., Delamere, W.A., 2007. The shape, topography, and geology of Tempel 1 from Deep Impact observations. Icarus 187, 4–15. http://dx.doi.org/10.1016/j.icarus.2006.12.013.

Vincent, J.B., Farnham, T., Kührt, E., Skorov, Y., Marschall, R., Oklay, N., El-Maarry, M.R., Keller, H.U., 2019. Local manifestations of cometary activity. Space Sci. Rev. 215, 30. http://dx.doi.org/10.1007/s11214-019-0596-8.

Vincent, J.B., Hviid, S.F., Mottola, S., Kuehrt, E., Preusker, F., Scholten, F., Keller, H.U., Oklay, N., de Niem, D., Davidsson, B., Fulle, M., Pajola, M., Hofmann, M., Hu, X., Rickman, H., Lin, Z.Y., Feller, C., Gicquel, A., Boudreault, S., Sierks, H., Barbieri, C., Lamy, P.L., Rodrigo, R., Koschny, D., A'Hearn, M.F., Barucci, M.A., Bertaux, J.L., Bertini, I., Cremonese, G., Da Deppo, V., Debei, S., De Cecco, M., Deller, J., Fornasier, S., Groussin, O., Gutiérrez, P.J., Gutiérrez-Marquez, P., Güttler, C., Ip, W.H., Jorda, L., Knollenberg, J., Kovacs, G., Kramm, J.R., Küppers, M., Lara, L.M., Lazzarin, M., Lopez Moreno, J.J., Marzari, F., Naletto, G., Penasa, L., Shi, X., Thomas, N., Toth, I., Tubiana, C., 2017. Constraints on cometary surface evolution derived from a statistical analysis of 67P's topography. Mon. Not. R. Astron. Soc. 469, S329–S338. http://dx.doi.org/10.1093/mnras/stx1691.